PCCP

Solvent Effect on the ^{195}Pt NMR Properties in Pyridonate-Bridged Pt^{III} Dinuclear Complex Derivatives by *ab Initio* Molecular Dynamics and Localized Orbital Analysis

Journal:	*Physical Chemistry Chemical Physics*
Manuscript ID	CP-ART-11-2020-005849.R2
Article Type:	Paper
Date Submitted by the Author:	08-May-2021
Complete List of Authors:	Rodrigues Batista, Patrick; University of Sao Paulo, Department of Fundamental Chemistry, Institute of Chemistry Ducati, Lucas; University of Sao Paulo, Department of Fundamental Chemistry Autschbach, Jochen; University at Buffalo, State University of New York, Chemistry

Solvent Effect on the ^{195}Pt NMR Properties in Pyridonate-Bridged Pt^{III} Dinuclear Complex Derivatives by *ab Initio* Molecular Dynamics and Localized Orbital Analysis

Patrick R. Batista,[a] Lucas C. Ducati,[a*] Jochen Autschbach[b*]
[a]Department of Fundamental Chemistry
Institute of Chemistry, University of São Paulo
Av. Prof. Lineu Prestes, 748
05508-000, São Paulo, SP, Brazil
[b]Department of Chemistry
University at Buffalo
State University of New York
Buffalo, NY 14260-3000, USA
*email: ducati@iq.usp.br
*email: jochena@buffalo.edu
May 12, 2021

Abstract: An *ab Initio* molecular dynamics investigation of the solvent effect (water) on the structural parameters, ^{195}Pt NMR spin-spin coupling constants (SSCCs) and chemical shifts of a series of pyridonate-bridged Pt^{III} dinuclear complexes is performed using Kohn-Sham (KS) Car-Parrinello molecular dynamics (CPMD) and relativistic hybrid KS NMR calculations. The indirect solvent effect (via structural changes) has a dramatic effect on the $^1J_{PtPt}$ SSCCs. The complexes exhibit a strong *trans* influence in solution, where the Pt−Pt bond lengthens with increasing axial ligand σ-donor strength. In the diaquo complex, where the solvent effect is more pronounced, the SSCCs averaged for CPMD configurations with explicit plus implicit solvation agree much better with the experimental data, while the calculations for static geometry and CPMD unsolvated configurations show large deviations with respect to experiment. The combination of CPMD with hybrid KS NMR calculations provides a much more realistic computational model that reproduces the large magnitudes of $^1J_{PtPt}$ and ^{195}Pt chemical shifts. An analysis of $^1J_{PtPt}$ in terms of localized and canonical orbitals shows that the SSCCs are driven by changes in the *s*-character of the natural atomic orbitals of Pt atoms, which affect the Fermi contact mechanism.

1 Introduction

Platinum–containing molecules or complexes are interesting probes to assess theoretical methods in the NMR parameters investigation of heavy elements because the ^{195}Pt (nuclear spin 1/2) has a wide chemical shift range (from -6000 ppm to 12000 ppm), depending of the oxidation state, donor or accepter characteristics of the coordinating ligand and of the metal–ligand interaction nature.[1,2] The scalar spin-spin coupling between ^{195}Pt and other magnetically active nuclei in solution may range from few Hertz to >140 kHz.[3]

The complexity involved in the calculations of the ^{195}Pt chemical shift and spin-spin coupling constants (SSCCs) makes very difficult to find an ideal computational model. Thus, the theoretical understanding of the observed experimental trends of ^{195}Pt NMR data remains a challenge. Among the main factors is the correct description of the chemical environment, such as the solvent effect, temperature, and pressure. Additionally, there is another hurdle to be considered, because heavy nuclei require relativistic methods to determine their magnetic properties,[4] which also increases the computational cost.

In particular, solvent effects are important because they can account for changes in the metal complex electronic structure and its geometry, resulting in detectable changes in physicochemical processes, reaction kinetics, and mainly NMR parameters.[5–8] For instance, Autschbach and Ziegler[9] showed for a set of Pt−Tl bonded systems that the magnitudes of the $^1J_{TlPt}$ coupling can be explained mainly due to the solvent coordination with the Tl atom and that the inclusion of explicit solvent molecules is underlying for a reasonable theoretical description of the experimental trends. However, the accuracy of the theoretical results of ^{195}Pt NMR data

can also be influenced by other factors, such as the internal reference, the density functional (in the case of density functional theory (DFT) calculations), and the basis set. A certain degree of error cancellation in the chemical shifts occurs when a compound chemically similar—and simulated in the same chemical environment—as the investigated systems is used as the internal reference for the calculations.[4,10,11] In part, such errors are related to the truncation of the basis set, the approximation of the electronic correlation by the density functional, and errors of self-interaction. Sterzel and Autschbach,[12] investigated chemical shifts of ^{195}Pt for a set of complexes in solution with different oxidation states as well as different coordination and solvation spheres. The goal was to minimize the potential for error compensation and thereby to expose the true difficulties with modeling platinum chemical shifts in an ab-initio fashion. The same study showed that explicit solvation is essential for a good agreement with the experimental data and that the ^{195}Pt NMR properties are strongly sensitive to the theoretical model. The authors also suggested that vibrational corrections may improve the accuracy of the calculated properties. More recently, Davis et al.[13] performed calculations of magnetic shieldings for the isotopologues and isotopomers of Pt^{IV} aqua/chlorido complexes with zero-point vibrationally averaged structures. Qualitatively, the trends of the observed effects were reproduced well, but the quantitative agreement of the calculated and experimental data was not reached. This was attributed to the implicit solvation model used. The inclusion of explicit solvent molecules seems to be imperative to obtain better results.

Among the oxidation states of Pt, +3 is more rare and, therefore, its NMR data is worthy of special attention. Mononuclear Pt^{III} compounds are unstable and very rare because of the reactive nature of the unpaired electron.[14,15] On the other hand, Pt^{III} dinuclear complexes are characterized by a structure involving a formal Pt−Pt bond resulting from the interaction between σ HOMO and σ^* LUMO orbitals derived from the symmetric and antisymmetric combination of d_z^2 orbitals of the metallic centers.[16,17] Typically known as platinum blue complex derivatives, they have Pt−Pt bridging ligands such as amidate,[18] acetate,[19] thiocyanates,[20] sulfates,[21] and phosphates,[22] connecting the two metal centers by NCO, NCS or OXO (X = C, S, P) moieties. From a structural perspective, Pt^{III} dinuclear complexes are classified as 'Head-to-Head' (HH), where the same platinum is coordinated to two nitrogen and two oxygen atoms of the ligands, generating two nonequivalent platinum atoms $Pt[N_2O_2]$ and $Pt[N_4]$. On the other hand, for the 'Head-to-Tail' (HT) arrangement, each equivalent platinum atom is coordinated to two different ligand atoms $Pt[N_3O]$.[23,24] Pt^{II} dimers, which show a large energy difference between σ HOMO and σ^* LUMO, leading to a less stable Pt−Pt bond, were also reported in the literature.[25]

The initial interest in platinum blue complexes was motivated by their potential action as drugs in the treatment of cancer,[26–28] especially after the discovery of cisplatin's antitumor

activity.[29–32] The ability to construct one-dimensional oligomeric chains, such as wires containing metal-metal interactions with mixed valence (Pt^{II} and Pt^{IV})[33–35], also drew attention for applications as light-emitting diodes, photovoltaic cells and molecular sensors.[36,37] In addition, interesting electrochromism,[35] photoluminescent, conductive, spectroscopic and catalytic properties have been found in these compounds in solution, where the role of the solvent may have a dramatic effect on the properties and behavior of the complex.[38–40] Still, the $^{195}Pt^{III}$ NMR parameters are also affected by the axial ligands and this can be, in part, explained by the cis/trans effect, likewise the Pt^{II} and Pt^{IV} complexes.[12,17,41–44] The solvent effect can account for changes of complex structure, influencing the electron density along the Pt−Pt bond in solvents of different polarities. Thus, the complexes may have a $L-Pt^{IV}-Pt^{II}-L$ character due to the polarization of the metal-metal bond, and it will be reflected on the NMR parameters of the metal center.

In the early 2000s, Bühl and coworkers applied molecular dynamics (MD) simulations to describe the solvent in NMR calculations, as an alternative to calculations that use static geometries. This approach proved to be successful in determining chemical shifts for metal complexes containing Fe,[45,46] Mn,[47] V,[48] and Co[49]. More recently, the combination of *ab initio* molecular dynamics (AIMD) based either on Born Oppenheimer molecular dynamics (BOMD) or Car-Parrinelo molecular dynamics (CPMD)[50] simulations followed by Kohn-Sham (KS) DFT calculations for light and heavy nuclei has been successfully applied to NMR parameter investigations in solution.[51–55] For instance, CPMD-based calculations with explicit solvation in the NMR calculations have been imperative for understanding the coordination regime of Tl with water molecules in Tl−Pt bonded complexes.[56] The $^{1}J_{TlPt}$ averaged out over the configuration trajectory reproduces the experimental data within the error bars of the chosen electronic structure model.[57] Based on natural molecular orbital (NLMO) analysis, the coordinating water molecules in the Tl site enhance the covalency of the metal-metal bond.

In the first reported study on platinum complexes applying AIMD,[58] Truflandier and Autschbach obtained ^{195}Pt nuclear magnetic shielding constants as an average over the CPMD trajectories with a small relative deviation of approximately 10% from the experimental data. A closely coordinated nonequatorial water molecule with the Pt^{II} and Pt^{IV} anionic complexes causes a pronounced solvent effect on the ^{195}Pt chemical shifts, which is correlated with the surface charge density. Furthermore, ^{195}Pt chemical shifts of neutral cisplatin derivatives in aqueous solution also showed a good agreement between theory and experiment with a deviation of approximately 5%.[59] Moreover, an investigation of the solvent effect on the SSCCs of neutral cisplatin showed that an inverse hydration, previously indicated as essential for reproducing the ^{195}Pt shielding tensor, also played a crucial role in the improved description of $^{1}J_{PtN}$ SSCCs.[60] However, there are still no studies related to the investigation of $^{195}Pt^{III}$ NMR data using

computational modeling of the chemical environment via AIMD.

Therefore, because AIMD is a powerful tool for obtaining dynamic molecular information in solution, the main goal of this work is to elucidate the dynamic solvent effect on the $^{1}J_{PtPt}$ SSCC and ^{195}Pt chemical shifts of $Pt^{III}-Pt^{III}$ bonded complexes, depicted in Figure 1, synthesized and characterized experimentally by Matsumoto and coworkers.[24,61–68] For this purpose, we combine the CPMD approach and relativistic KS-DFT NMR calculations. This high-level modeling of the solvent effects on the electronic structure as well as the solvent-solute interactions on the structural parameters is necessary, due to the aforementioned difficulties in reproducing experimental ^{195}Pt NMR parameters with good accuracy by calculations. The effects of coordinating solvent molecules on the NMR parameters are rationalized by means of NLMO analysis. The selected Pt−Pt bonded systems are interesting in terms of their potential applications, and present a very challenging test case to see how far the theoretical methods can be pushed at present.

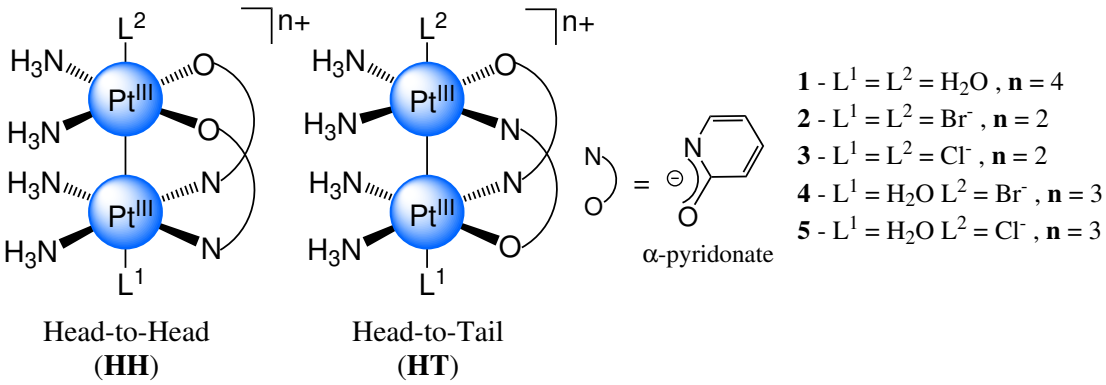

Figure 1: Head-to-Head (HH) and Head-to-Tail (HT) Pt-Pt α-pyridonate-bridged complexes.

2 Computational Details

CPMD simulations were performed using the plane wave (PW), periodic boundary DFT code Quantum ESPRESSO (QE) version 6.0.[69] NMR SSCCs and chemical shifts were computed using the CPL[70–72] and NMR module[73–75], respectively, of the Amsterdam Density Functional (ADF) package,[76] version 2017.[77]

The geometries of complexes **1-5** were optimized using the PW module of QE. The simulations consisted of a single optimized complex placed in the center of a cubic cell and packed with water and counter ion molecules. The experimental sample solution for NMR measurements was prepared using an acidic D_2O solution ($DClO_4/D_2O$) to suppress deprotonation of the complex ligands.[24]. Thus, perchlorate anions (ClO_4^-) were added taking

into account the charge of each complex, in order to maintain the neutrality of the cell and a total of 64 solvent molecules (water + perchlorate anions). All hydrogen atoms were replaced with deuterium to aid in adiabatic separation of the electronic and nuclear degrees of freedom.[78] Cell dimensions, L, were chosen such that the density of the system was equal to that of the heavy water at ambient conditions. The specific parameters for each system were as follows: **1**: complex + 60 water molecules + 4 perchlorate anions; L = 15.40 Å; **2**: complex + 62 water molecules + 2 perchlorate anions; L = 15.51 Å; **3**: complex + 62 water molecules + 2 perchlorate anions; L = 15.30 Å; **4**: complex + 61 water molecules + 3 perchlorate anions; L = 15.55 Å; **5**: complex + 61 water molecules + 3 perchlorate anions; L = 15.45 Å. The initial configurations were constructed with PACKMOL package[79,80]

Structure optimizations and CPMD simulations were performed with the Perdew, Burke, and Ernzerhof (PBE) generalized gradient approximation (GGA) exchange-correlation functional.[57,81] Ultrasoft pseudopotentials available from psilibrary 1.0.0[82] were used to represent effective nuclei. A kinetic energy cutoff of 100 RY was found to be suitable, providing an energy convergence of better than 2 meV per atom. Grimme's dispersion correction (D2)[83] was included for all atoms. A fictitious electron mass of 450 au and a time step of 5.0 au (0.12 fs) were used for their stability in integrating the CPMD equations of motion.[50,84,85] After an initial wave function optimization (using the CP module of QE), two simulation steps were performed, i.e., equilibration and production trajectories. Equilibration was conducted in the canonical ensemble (NVT) using a Nosé-Hoover thermostat[86] with a target temperature of 350 K. The elevated temperature is known to alleviate deviations from the experimentally observed structure of pure water compared with water simulations in CPMD that would otherwise occur.[78,87–89] The systems were allowed to equilibrate for approximately 3 ps before the thermostat was turned off. The production followed the equilibration trajectory in the microcanonical ensemble (NVE) for 30 ps. The first 1 ps in the NVE ensemble was considered part of the equilibration. The reliability of CPMD was probed by calculating radial distribution functions (RDFs) and selected mean distances and angles for the solute. These calculations were performed with 2000 CPMD configurations from the production step with a maximum radius (r_{max}) of 12 Å and a discrete radial grid of 0.03 Å, provided by Visual Molecular Dynamics (VMD),[90,91] version 1.9.3.

The chemical shifts of ^{195}Pt and $^{1}J_{\mathrm{PtPt}}$ SSCC calculations were performed with the hybrid PBE0 functional (containing 25% exact exchange)[57,92] including only scalar relativistic (SR)[70] or scalar and spin-orbit (SO)[71] relativistic effects by means of the zero-order regular approximation (ZORA)[93] Hamiltonian.[94] ZORA has been shown to be accurate for treating the relativistic effects impacting NMR chemical shifts and J-coupling.[95,96] Comparison with other relativistic methods, such as the fully relativistic four-component approach, linear response elimination of small component (LR-ESC) and four-component Dirac-Kohn-Sham (DKS) theory, have also

demonstrated that ZORA is accurate for chemical shifts and *J*-coupling, even when very heavy elements are involved.[97,98] We note in passing that ZORA is not accurate for absolute shielding. However, this is not relevant in the context of the present work. The augmented all-electron STO basis, developed for *J*-coupling calculations (jcpl)[57] was used for Pt atoms, and other atoms were described by an all-electron Slater-type orbital (STO) basis set of polarized valence triple-ζ (TZP) quality. In addition to the presence of explicit solvent molecules, the conductor-like screening model (COSMO)[99] was applied. The level of theory was chosen as a compromise between the computational cost and accuracy for the dynamics of aqueous systems.[56,78] The hybrid functional is more suitable for NMR parameter calculations because it reduces the self-interaction error in semilocal DFT and thereby furnishes a more accurate and reliable description of the electronic structure in the systems of interest.[57,100,101]

The SSCC calculations were initially performed with ZORA-SR using 64 evenly spaced (every 0.45 ps) CPMD configurations from the production trajectory to provide a coarse estimate of the cluster size (number of nearest neighbor (NN) solvent molecules to include in addition to the solute) for each system. Solvent molecules were added around the solute from 0 to 25 in sets of 5, with and without COSMO in each selected CPMD configuration. The selection of NNs was performed using a Fortran90 code developed in our group, which creates a 3 by 3 by 3 supercell of the periodic simulation cell of each frame of interest. From this super cell, interatomic distances were compared with covalent radii plus a small additional factor (following typical conventions for semiempirical bond drawing)[102] to determine molecular subunits. The criterion for choosing NN solvent molecules was based on the increasing order of interatomic contacts between the solute and solvent. The absence of explicit or implicit solvation was also considered using only the solute geometries of each CPMD configuration without COSMO.

Thus, the dependence on magnetic properties as a function of the number of explicit solvent molecules was analyzed averaging out the SSCCs. Furthermore, the coupling constants were decomposed in terms of localized molecular orbital (LMO) contributions in a relativistic *J*-coupling analysis[56] with natural LMOs (NLMOs) with the natural bond orbital (NBO) program version 6.0 included in the ADF package.[103] In this analysis, a set of localized orbitals, NBOs and NLMOs, is determined from SR electronic structure while the property is calculated including all relevant SO coupling terms. The projection of the SO orbitals onto the *full* (occupied and unoccupied) set of SR orbitals affords the link between the two set of orbitals. The sum of all terms in the analysis is therefore equal to the NMR parameter calculated from variational SO DFT, allowing a decomposition in terms of SR localized orbitals, being easy-to-interpret and easy-to-visualize.[104,105]

After the required NN solvent molecules were determined for SSCC convergence, 192 additional configurations were selected for improvement of the statistical averaging, i.e., the final

statistics were accumulated from 256 configurations per complex, evenly spaced over the production trajectory (every 0.11 ps). Based on the required NN explicit solvent molecules, the SSCCs and ^{195}Pt shielding tensors were computed with a ZORA-SO Hamiltonian for all 256 clusters. The chemical shifts were calculated from isotropic shielding constants and experimental shifts using eqn (1),

$$\delta_{\mathrm{calc}} = \sigma_{\mathrm{ref}} - \sigma_{\mathrm{probe}} + \delta_{\mathrm{ref}}^{\mathrm{exptl}} \quad (1)$$

Here, $\mathbf{1}^{\mathrm{HH}}$ was used as a secondary reference 'ref' in the calculations, and the experimental chemical shift of $\mathbf{1}^{\mathrm{HH}}$ with respect to aqueous H_2PtCl_6 was added to convert the calculated shifts to the standard reference. This commonly used way of referencing calculated chemical shifts avoids systematic errors from having the probe and reference nucleus in different oxidation states or in very different chemical environments.[12]

3 Results and Discussion

3.1 Assessment of solvent

It is well known that the pure functionals, such as the PBE used in this work, overestimate the hydrogen bond energy,[78] causing a 'glassy' character of water. This effect is manifested as a higher O-O first peak and a deeper first trough in the oxygen-oxygen (*g(r)*OO) RDF when compared to RDFs obtained from neutron scattering and/or X-ray diffraction experiments.[106–108] However, the simulations performed at 350 K with Grimme's dispersion correction (D2) minimize such an overstructuring effect. The increase in the simulation temperature also mimic the nuclear quantum effect in structural quantities such as the *g(r)*OO RDF, which is known to be essential for accurate description of microscopic structure of liquid water.[109] The solvent structure in the simulation was analyzed from the *g(r)*OO RDFs of the HH complexes given in Figure 2 and compared with the experimental (full orange line) and simulated (full red line) RDFs of pure liquid water.

The first set of peaks from 2.20 Å to 2.45 Å refer to solute (O_{sol}) and solvent (O_{solv}) oxygen atom pairs. Complexes with diaquo ligands (**1**, **4** and **5**) present sharper intensity peaks due to hydrogen bonds between the solvent and ligands. The second set of peaks from 2.45 Å to 6.00 Å presents a small shift and overstructuring (zoom in Figure 2) caused in part due to the presence of the large solute complexes, which reduce the solvent mobility due to solute-solvent interactions. However, based on the experimental uncertainties,[106–108,110,111] the simulated *g(r)*OO reflect a reasonably accurate simulation of the intermolecular structure of liquid water. The same features were observed for the *g(r)*OO of the HT complexes (Figure S2 in SI).

Additionally, RDFs *g(r)*HH are depicted in Figures S3 and S4 and likewise agree reasonably well with the experimental data for pure liquid water.

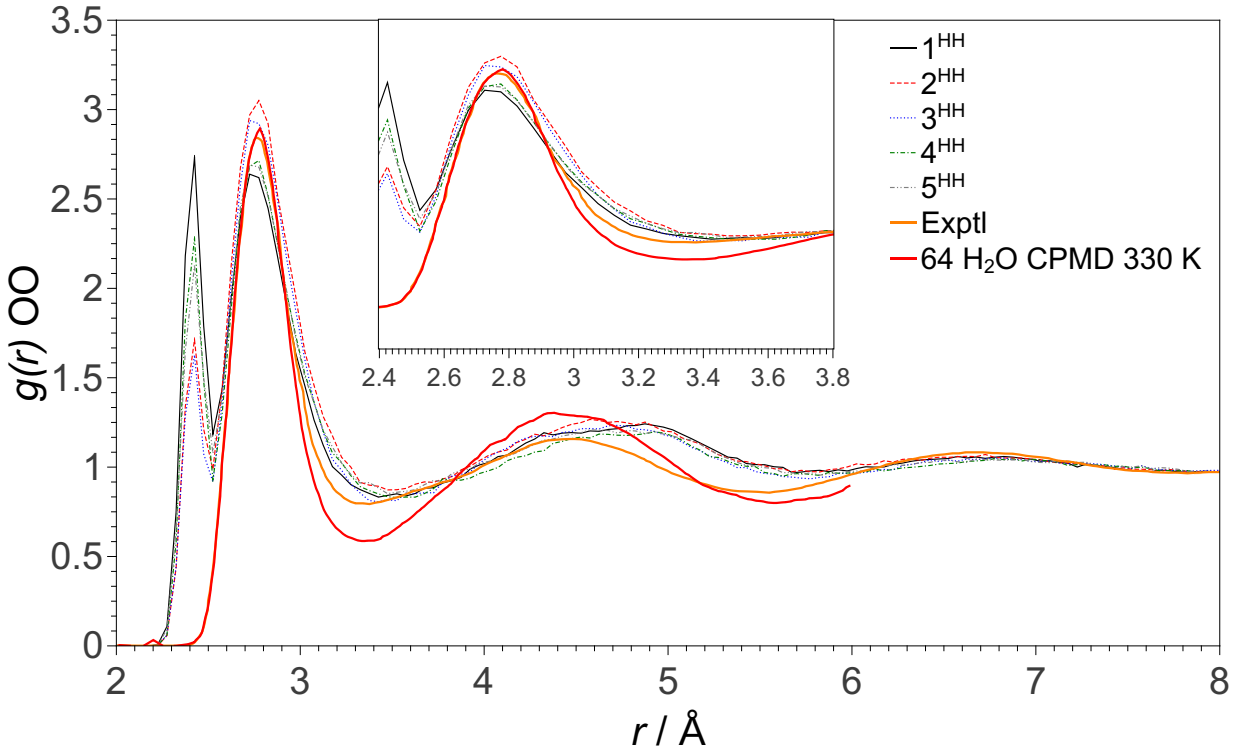

Figure 2: Oxygen-oxygen RDFs for each of the five explored HH Pt(III) complexes; *g(r)*OO denotes the RDF or pair correlation as a function of pair distance in Å. The full orange line is the experimental oxygen-oxygen RDF for heavy water from the joint X-ray diffraction and neutron scattering experiments of Soper and Benmore[111]. The full red line is the theoretical oxygen-oxygen RDF for pure water obtained by CPMD at 330 K[109]. These latter two were extracted using the engauge plot digitizer.[112]

3.2 Dynamic Properties

In order to analyze the mobility of the simulated systems, the root mean square deviation (RMSD) for the perchlorate anions Cl atoms and water molecules O atoms were computed relative to the initial frames of the production trajectory. The RMSD plots are given in Figure S5. The RMSD shows a diffusive behavior for the water molecules and perchlorate anions throughout the simulation. In addition, the average distances between the Cl atoms and Pt atoms were calculated (see Table S1 for specific values of each simulation) to assess how far the perchlorate anions are from the solute on average, during the simulation. The distance between the perchlorate anions and the solute is 9.8 ± 0.7 Å, 6.8 ± 0.6 Å and 7.7 ± 0.4 Å on average for diaquo, dihalo and aquahalo complexes, respectively. This shows that the counter ions can be found surrounding the

solute at a distance, equal or greater than the half of the simulation box, i.e, $L/2 = 7.70 \pm 0.05$ Å on average. Therefore, the solvent-separated ion pair in aqueous solution is correctly reproduced by the simulations.

3.3 Solute Structures and Solvation Shell

The platinum-oxygen RDFs describe the structure of oxygen atoms radially outward from each platinum atom. The HH complexes were separately calculated because of the platinum atom asymmetry with respect to the ligand bond lengths, which are the average of the two platinum atoms for the HT complexes. Figure 3 shows the RDFs *g(r)*Pt[N_4]O and *g(r)*Pt[N_2O_2] and their integration for the five HH complexes studied in this work. The RDFs and their integrates for HT complexes are depicted in Figures S6 and S7 in the Supporting Information (SI) because they presented similar features to those discussed herein.

The first set of peaks from 2.0 Å to 2.6 Å in Figure 3A represents the axial oxygen of the aquo ligand for the diaquo and aquahalo complexes. The shape of these peaks indicate a direct coordination of oxygen atoms to Pt atoms and the strength of the Pt-OH_2 bond. Therefore, the $g(r)_{max}$ of the peaks of aquahalo complexes is slightly smaller because of a weaker Pt-OH_2 bond in comparison with the diaquo complex. The set of peaks at $r \sim 3.1$ Å corresponds to the equatorial oxygen bonded to the Pt[N_2O_2] atom for all complexes. The third and fourth sets of peaks represent oxygen atoms from solvent molecules contained at the first and second solvation shells at $r \sim 4.2$ Å and 6.2 Å, respectively. Similarly, the first set of peaks represents the axial and equatorial oxygen atoms bonded to the Pt[N_2O_2] atom for the five complexes in Figure 3C. The second and third sets of peaks, between 3.6 Å and 7.0 Å, depict oxygen atoms from solvent molecules of the first and second solvation shells. The RDFs show no structure at approximately 7.0 Å.

RDF integration (Figures 3B and 3D) provides, on average, the number of oxygen atoms at a distance *r* from a platinum atom, considering the oxygen atoms explicitly coordinated on platinum sites and the number of water molecules in the solvation shells. In the RDF integrals, the atoms from the previous radial shell are summed to the number of atoms of the next one because the solvation shell consists of all solvent molecules within the respective radius.

For Pt[N_4] of diaquo and aquahalo complexes, the first radial shell has a single oxygen atom, while in the second radial shell, there are two oxygen atoms. At the same distance, the first two water molecules are near this Pt site for the dihalo derivatives (Figure 3A). Three oxygens are found in the first radial shell of the Pt[N_2O_2] atom (Figure 3C) for the diaquo complex, comprising two equatorial ligands and one axial ligand. For dihalo and aquahalo complexes, only the oxygen from equatorial ligands is counted.

The RDF integration shows 10 and 30 solvent molecules on average within the first and second

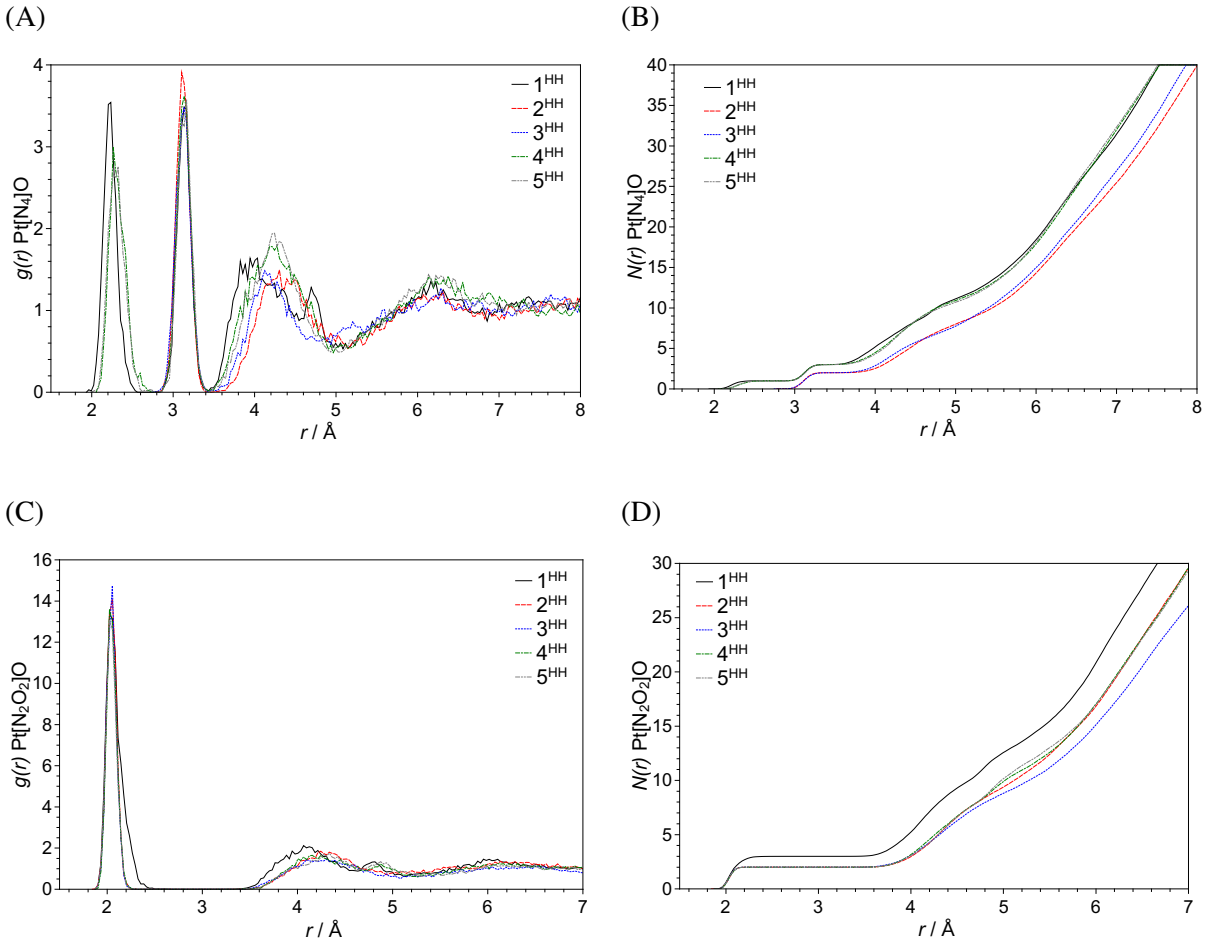

Figure 3: Platinum-oxygen RDFs and their integrates for 2000 configurations of the production trajectories of the five explored HH Pt(III) complexes. *g(r)*Pt[N_4]O and *g(r)*Pt[N_2O_2] denote the RDFs or pair correlations as a function of pair distance in Å; *N(r)*Pt[N_4]O and *N(r)*Pt[N_2O_2]O denote the RDF integrates.

solvation shells, respectively. Thus, a total of 64 solvent molecules included in the cubic box for simulation is sufficient to describe the complexes in solution. Furthermore, visual inspection of the trajectory reveals that the water molecules are located close to the equatorial NH_3 and axial OH_2 ligands, interacting by hydrogen bonds. An example with a configuration of the HH diaquo complex is provided in Figure 4.

The visual inspection also reveals important changes in the L−Pt−Pt−L moiety of the diaquo and aquahalo complexes, which may influence the ^{195}Pt NMR properties. The strong dynamic interaction of the aquo ligands with solvent molecules induces an axial elongation of the Pt-OH_2 bonds to a maximum length of 2.47 Å for Pt[N_4]-OH_2 and 2.33 Å for Pt[N_2O_2]-OH_2. On the other hand, while the bond of the aquo ligands becomes shorter, the Pt−Pt bond undergoes a dynamic

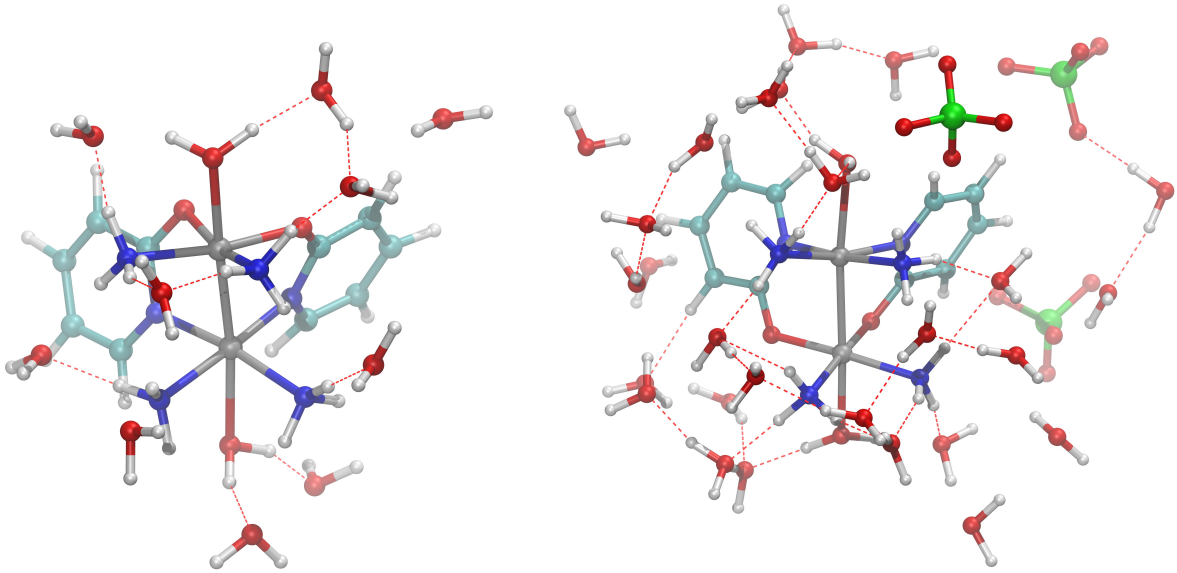

Figure 4: Snapshot from the production trajectory of the HH diaquo complex showing the first solvation shell with 10 solvent molecules (left) and the first plus the second solvation shell with 30 solvent molecules (right). The dashed lines represent the hydrogen bonds based on classical criteria.[113] Note that in the simulation the counter ions visible in larger cluster are fully solvated.

axial lengthening (until reaching the maximum length of 2.73 Å) in a synchronous motion opposite to the axial bonds.

In addition to structural solvation, the complexes were also characterized with respect to their geometric parameters in solution. The mean interatomic distances, angles and dihedrals, averaged over the production trajectories, are listed in Tables S2 and S3. The available experimental data from X-ray crystal structures[114–116] were included. The Pt−Pt average bond length ranges from 2.594 Å to 2.635 Å. This indicates the presence of formal metal-metal bond between two d^7 metal ions, because the Pt−Pt bond generally varies from 2.500 Å to 2.700 Å,[117] in dinuclear platinum(III) complexes. The angles of the L−Pt−Pt−L moiety show a units of degrees deviation, whereas the dihedral angles have a large deviation from the experimental ranges, even for the static bare structure. The evolution of the main bond lengths and distribution of dihedral angles during the simulation are depicted in Figure 5 for HT complexes, which were chosen because of their bridging ligand symmetry, where the influence of α-pyridonate ligands may be avoided.

Overall, the Pt_1-Pt_2, Pt_1-L_1 and Pt_1-L_2 bonds are lengthened in the order diaquo < dichloro < dibromo. For the aquahalo complexes, the Pt_1-Pt_2 bond increases in the order aquachloro < aquabromo, while no substantial difference was found in the $Pt-OH_2$ bond lengths for both complexes. The Pt_1-Pt_2 bond lengthens by 0.031 Å and 0.059 Å upon changing the axial ligands

from aquo to chloride and from aquo to bromide, respectively. Thus, when chloride is replaced by bromide, the Pt_1-Pt_2 bond becomes 0.028 Å longer. As expected, in the aquahalo complexes, the Pt_1-Pt_2 bond has an intermediate length between those of the diaquo and dihalo complexes, increasing on average by 0.018 Å. Furthermore, it is important to note that the mean Pt−Pt bond length in the aquachloro complex is only 0.003 Å longer than in the aquabromo complex. These results suggest that the complexes present a strong *trans* influence effect in solution, where the Pt−Pt bond lengthens with increasing axial ligand σ-donor strength in a fashion consistent with the established structural *trans* influence series in mononuclear platinum complexes.[41–43,118] This effect arises from the polarization of the shared metal atomic orbital, induced by one of the substituents, which consequently causes a repolarization of the same orbital in the trans position.

The axial average Pt−ligand bond length also changes in solution because of hydrogen bonds between ligands and solvent molecules as well as the *trans* effect. For dihalo complexes, the Pt−Cl (2.513 Å and 2.495 Å) and Pt−Br (2.649 Å and 2.645 Å) bond lengths are >0.1 Å longer than the experimental data and longer than the typical Pt−Cl and Pt−Br bond distances for platinum(II) and platinum(IV) structures.[58] The effect of changing the axial ligands on the chemical bonds can be observed in Figure 5 trough the overlap of the evolution bond lines. Upon replacing aquo ligands by chloride (top-right), the average Pt−Cl bond lengths are very close to the Pt−Pt bond length. Furthermore, when aquo ligands are replaced by bromide (middle-left), the metal-metal and metal-ligand bonds have the same average lengths. Likewise, in aquahalo complexes, Pt_2-Br is 0.155 Å longer than Pt_2-Cl, and the mean Pt_1-OH_2 bond length is 2.280 Å for both complexes. These results indicate that the Pt−Pt bonds in the aquahalo complexes are more polarized than those of the diaquo and dihalo complexes. Similiar results were obtained for platinum(III) acetate-bridged dimers with axial halide ligands in the solid state, where the metal-ligand bond lengthens more than 0.1 Å because of the *trans* effect.[17] Additionally, the *trans* effect for HH α-pyridonate-bridge compounds is responsible for lengthening the Pt−Pt bond by 0.024 Å when chloride is replaced by bromide, as probed via X-ray structures.[116,119]

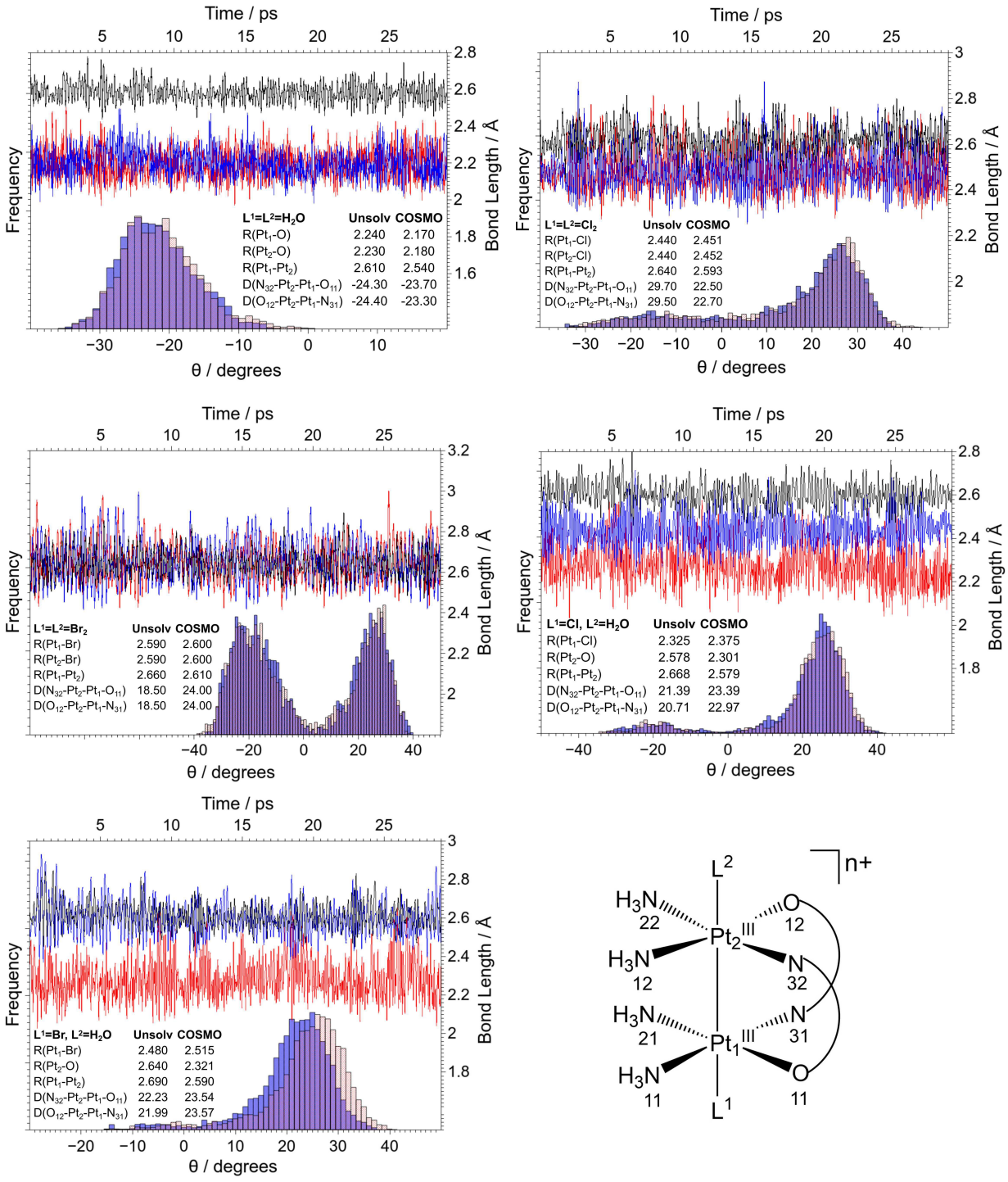

Figure 5: Dynamic evolution of selected geometrical parameters for the HT diaquo (top-left), dichloro (top-right), dibromo (middle-left), aquachloro (middle-right) and aquabromo (bottom-left) complexes: evolution of Pt_1-Pt_2 (black line), Pt_1-L^1 (red line) and Pt_2-L^2 (blue line) bonds during the CPMD simulation, along with the $N_{32}-Pt_2-Pt_1-O_{11}$ (blue histogram) and $O_{12}-Pt_2-Pt_1-N_{31}$ (red histogram) dihedral angle distributions. Values inside the graphs are the bond lengths (R), and dihedral angles (D) for complexes calculated using unsolvated and implicitly solvated (COSMO) optimized static geometries.

Interestingly, Figure 5 shows that the distribution of the torsional angle around the Pt−Pt bond is Pt−L dependent. For the diaquo complex (top-left), both dihedral angle distributions show a restricted feature with substantial probability for angles near -22°, favoring the *synclinal* conformation. The distributions are more diffuse with small probabilities for angles in the range of 5° to -30°, when aquo ligands are replaced by chloride (top-right). Additionally, geometries present the eclipsed conformation when angles of approximately 22° are more often visited. On the other hand, replacing chloride with bromide (middle-left), the distributions are more restricted again, presenting two symmetry probability angles. Therefore, because of the *trans* effect, the increase in Pt−Pt bond length improves the rotational ability around the bond, decreasing the steric repulsion between the NH_3 ligands and increasing the probability for a *synclinal* geometry. Nonetheless, visual inspection reveals that the bridging ligands symmetry contribute to two eclipsed octahedrals (Figures 6A and 6B, where the *trans* effect is known to be more pronounced.

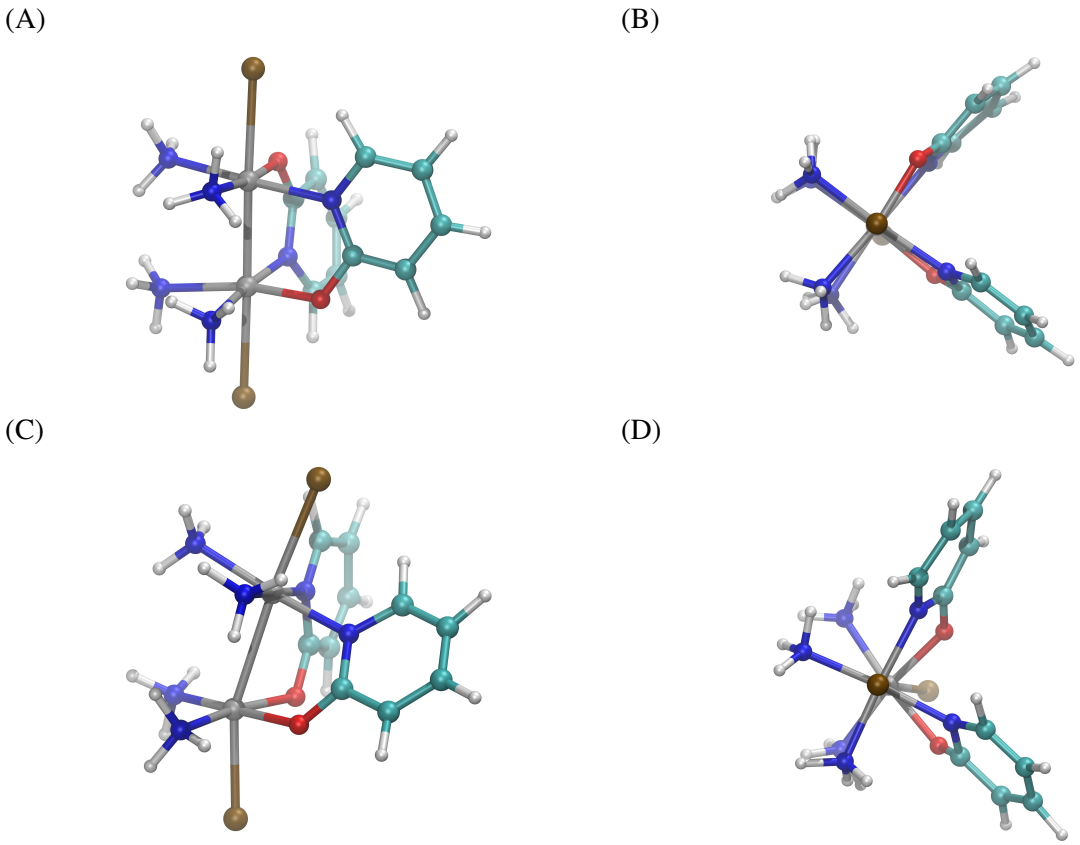

Figure 6: Snapshots from the production trajectory of the HH and HT dibromo complexes showing the pseudooctahedral geometries in the CPMD simulation: side view (**A**, **C**) and top view (**B**, **D**). The geometry of the HT complex is in good agreement with the two eclipsed octahedrals. The bridging ligand asymmetry in the HT complex yields a twisted geometry when the Pt-Pt bond lengthens.

For the aquahalo complexes, the dihedral angles present differences with respect to the axial ligand *trans* effect. In the aquachloro complex (middle-right), the dihedral distributions are somewhat less diffuse than in the dichloro complex (top-right) and the aquabromo complex (bottom-left). These complexes have more restricted dihedral distributions with a significant probability for angles of approximately 25° with respect to the dibromo complex (middle-left). Therefore, more than one effect may be at work in aquahalo complexes as a competition between aquo ligands (weak σ-axial donor) and halide ligands (strong σ-axial donors), as well as the polarization of metal-metal bonds, such as $X{-}Pt^{IV}(N_3O){-}Pt^{II}(N_3O){-}OH_2$.[24]

For HH complexes where the bridging ligands are not symmetrically bonded on the platinum atoms, similar features were observed in diaquo, dichloro and aquachloro complexes, with some differences due to their own asymmetry, which appears to slightly decrease the *trans* effect. In complexes with bromide ligands (dibromo and aquabromo) and the HT systems, the *trans* effect

is more pronounced. However, the rotation around the Pt−Pt bond, probed by dihedral angles, does not occur easily because the solute has a twisted geometry (Figures 6C and 6D) when the Pt−Pt bond is elongated because of the bridging ligand asymmetry. Therefore, the solute structural features in solution noted here may indeed be crucial for NMR parameter calculations of the systems studied in this work, as suggested by Sterzel and Autschbach[12].

3.4 Pt^{III}–Pt^{III} Spin-Spin Coupling Constants - $^1J_{PtPt}$

Initially, the effect of relativistic corrections on the $^1J_{PtPt}$ calculations was evaluated with ZORA-SR and ZORA-SO Hamiltonians. Thus, the $^1J_{PtPt}$ calculations were performed using an evenly spaced set of 64 configurations from the production trajectory for the HH diaquo complex. In addition, the number of NN solvent molecules was included in increments of five, along with COSMO to treat bulk solvent effects. The bare-solute regime was also considered to assess only the thermal effects on the selected configurations. Figure 7 shows a profile of $^1J_{PtPt}$ average values regarding explicit solvation and the relativistic corrections applied.

The profiles of the two curves are very similar, with both converging at ten NN solvent molecules. Furthermore, the difference between the results for the ZORA-SR and ZORA-SO Hamiltonians was quite substantial (approximately 22%), and despite the overestimation of the calculated $^1J_{PtPt}$ the SO effect must be considered for the magnetic property calculations of the complexes studied. However, the ZORA-SR/PBE0/jcpl level of theory was applied to investigate the solvent effect on $^1J_{PtPt}$ coupling to reduce the computational cost. These results are shown in Figure 8 based on the data given in the SI (Table S4).

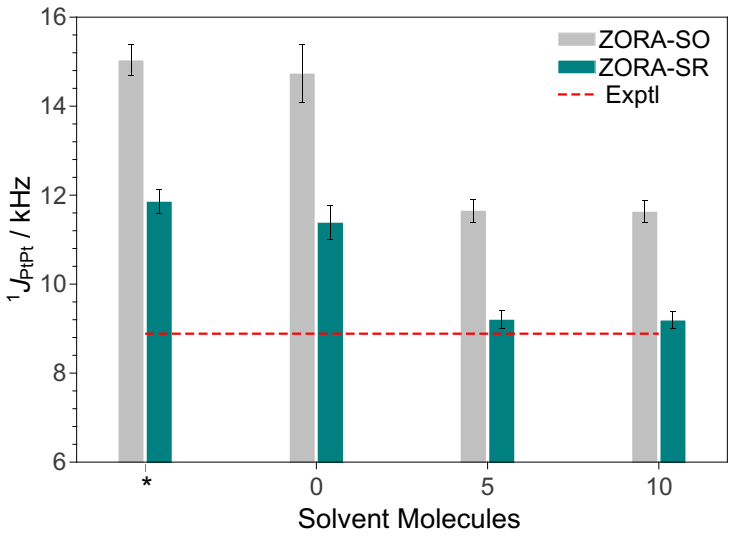

Figure 7: $^1J_{PtPt}$ dependence profile of the HH diaquo complex on the explicit NN solvent count and relativistic corrections. All data are means corresponding to production trajectory averages (64 configurations). The asterisk correspond to bare structures (no explicit or implicit solvation), while the remaining counts (0-10) correspond to structures including the given number of explicit nearest solvent molecules and implicit solvation via COSMO. Bars in each point are the standard errors in the means.

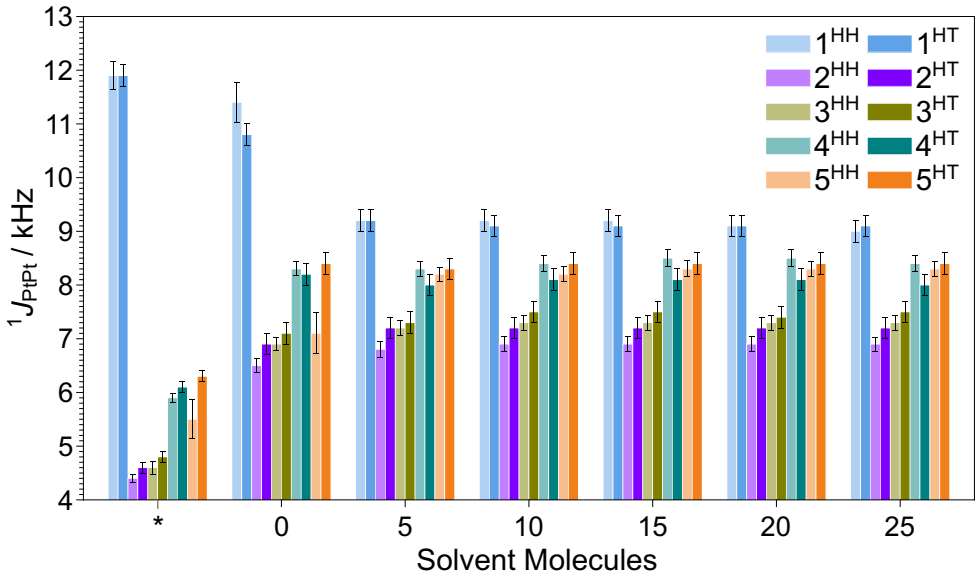

Figure 8: $^1J_{PtPt}$ dependence on the explicit NN solvent count for complexes 1-5, Head-to-Head (HH) and Head-to-Tail (HT). All data are means corresponding to trajectory averages (64 frames). The asterisk correspond to bare structures (wherein all solvent molecules were stripped and without implicit solvation), while the remaining counts (0-25) correspond to structures including the given number of explicit nearest neighboring solvent molecules and implicit solvation via COSMO. Standard errors (in the means) are given by the solid black lines.

Figure 8 shows the solvent dependence of the Pt−Pt coupling for all complexes. Overall, the trends show that, as the solvent molecule count increases, the Pt−Pt coupling constants decrease until convergence for the diaquo complex while increasing toward solvation for the dihalo and aquahalo complexes. Additionally, the implicit solvent has proven to be effective in changing the calculated *J*-coupling, specifically when comparing CPMD bare structures (*) and CPMD structures only with COSMO solvation ('0'). For dihalo and aquahalo complexes, the average of $^{1}J_{PtPt}$ converged when 5 NN solvent molecules were present. However, for diaquo complexes, at least 10 NN solvent molecules are required to achieve convergence because they have a pronounced interaction with the solvent via hydrogen bonds through aqueous ligands, which undergo exchange by solvent water molecules.

Therefore, to maintain rigorous solvation criteria for all complexes, 10 NN solvent molecules were considered to calculate the SSCCs with the ZORA-SO/PBE0/jcpl level of theory, i.e., around the first solvation shell according to the RDFs *g(r)*Pt[N_4]O and *g(r)*Pt[N_2O_2] in Figure 3 and Figures S6 and S7 .

3.4.1 Configuration sampling

To obtain the magnetic properties with statistical reliability, it is necessary to sample the total configurations generated by the CPMD. However, such sampling must be performed systematically, guaranteeing the number of configurations necessary, resulting in data with a satisfactory degree, and representing the complete simulation.[120] This result can be verified by the evolution of the average value for a given property with respect to the number of configurations. As mentioned in the Computational Details section, a total of 256 configurations evenly spaced from the production trajectory were selected to calculate the average magnetic properties.[58] Figure S13 shows that the evolution of the average of $^{1}J_{PtPt}$ converges with approximately 200 configurations, guaranteeing the sampling 256 configurations is representative.

Based on Configuration sampling, the final SSCC averages along the CPMD trajectories, using 256 configurations with different solvated and unsolvated models, are collected in Table 1. In the Unsolvated and COSMO models, the static geometry with and without implicit solvent is used, respectively. In the CPMD-Bare model, all solvent molecules were stripped of the configurations from production trajectory and without implicit solvation (COSMO). Explicit and implicit solvation are then included in the CPMD model.

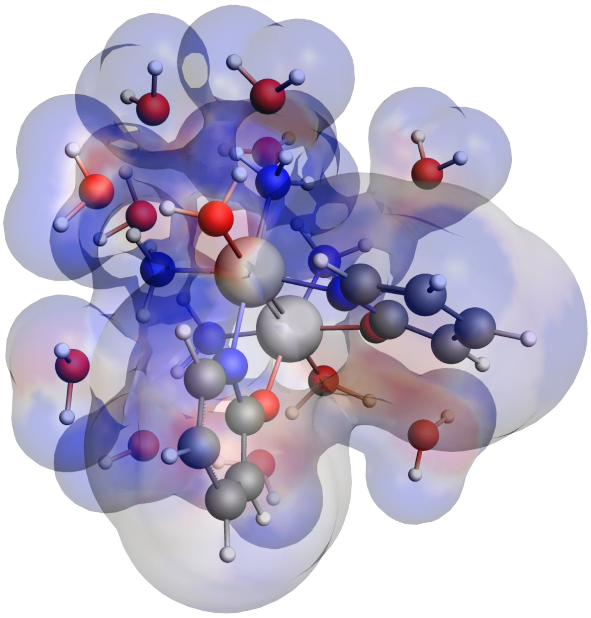

Figure 9: Depiction of the solvent-accessible surface for the continuum solvent model COSMO for a snapshot from the production trajectory of the HH diaquo complex with 10 explicit solvent molecules. Red, gray, and blue regions on the surface correspond to negative, neutral, and positive potentials, respectively.

The results highlight the dependence of the solvent effect on the Pt−Pt coupling constant calculations. For the diaquo complexes, where the solvent effect is more pronounced, the COSMO model leads to SSCC approximately 6% and 38% lower than those of the Unsolvated for optimized static geometries of the HH and HT systems, respectively. The CPMD-bare provides SSCC 25% (for HH) and 30% (for HT) lower than those of the Unsolvated model, indicating that the indirect solvent effect (vibrational contributions and structural changes) also contributes substantially to the $^{1}J_{\mathrm{PtPt}}$ coupling accuracy. However, the SSCCs remain more accurate, approximately 22% lower than in the CPMD-bare by including explicit and implicit solvation (referred to as CPMD). The CPMD reduces the calculated SSCC, on average, by 43% with respect to those of unsolvated static geometries, although the results remain slightly overestimated. Thus, SSCCs averaged on CPMD configurations with 10 NN solvent molecules plus COSMO provided a deviation of 31% from the experimental, while the Unsolvated and CPMD-Bare models show deviations of 125% and 69%, respectively. Therefore, representing bulk solvation via COSMO along with the explicit first solvent shell is very important because it modifies the properties of the explicit solvent molecules, as shown in the next section. Figure 9 shows one of the 256 snapshots used in computing the J-coupling for the HH diaquo complex in Table 1. Overlaid in this image is the solvent-accessible surface generated from the COSMO radii, with the surface colored by the corresponding COSMO potential.

Table 1: Calculated $^1J_{PtPt}$ spin-spin coupling constants[a] for Head-to-Head (HH) and Head-to-Tail (HT) complexes 1-5 with different solvated and unsolvated models. $^1J_{PtPt}$ calculations were performed at the PBE0/ZORA-SO/TZP(jcpl) level of theory. The values in square brackets are the relative error regarding the experimental data.[b]

Complex	Unsolvated[c]	COSMO[d]	CPMD-Bare[e]	CPMD[f]	Exptl[g]
1^{HH}	19971 [125]	18843 [112]	15037 [69]	11633 [31] (11629)	8886
1^{HT}	20979	13048	14751	11694 (11556)	——
2^{HH}	5578 [-12]	7921 [26]	5140 [-18]	8680 [38] (8553)	6306
2^{HT}	6320	8157	5418	9571 (8988)	——
3^{HH}	5922 [-11]	8285 [25]	5574 [-16]	9275 [40] (9236)	6636
3^{HT}	5956	8494	5771	8941 (9477)	——
4^{HH}	7358 [-3]	9694 [28]	6561 [-13]	10520 [39] (10558)	7574
4^{HT}	8014 [10]	10129 [40]	6981 [-4]	10566 [46] (10086)	7260
5^{HH}	7649 [-2]	10752 [38]	6686 [-14]	10413 [34] (10328)	7774
5^{HT}	8924 [18]	10249 [35]	7495 [-1]	10291 [36] (10648)	7564

[a]Hz. [b]%. [c]Relativistic couplings from the unsolvated, relativistically optimized geometry. [d]Relativistic couplings from the relativistically optimized geometry with implicit solvation. [e]Average of 64 CPMD configurations, wherein all solvent molecules were stripped and without implicit solvation. [f]Average of 256 CPMD configurations plus a specified number of explicit nearest neighboring solvent molecules and implicit solvation to model the bulk effect. The values in parentheses are the average of 64 CPMD configurations. [g]Measurements using an acidic D_2O solution ($DClO_4/D_2O$) to suppress deprotonation of the diaqua complexes. Data extracted from Iwatsuki and coworkers.[24]

For the dihalo and aquahalo complexes, the COSMO effect on the static geometry causes an increase in the calculated $^1J_{PtPt}$ of 38% and 28% on average, respectively. CPMD-Bare structures provide similiar results for an unsolvated static geometry when compared to the experimental data. These characteristics can be rationalized considering the electrostatic, 'semiclassical' vibrational and solvent contributions to the NMR properties. The electrostatic contribution is predominant in the static regime with COSMO and the 'semiclassical' vibrational and solvent contributions appear in the CPMD approach resulting from the classical thermal motion of the nuclei (see also refs. 58 and 59) and the presence of the explicit solvent molecules, respectively. Thus, the results suggest that the vibrational contribution, which predominate in the CPMD-Bare, is opposed to electrostatic contribution from COSMO. In some cases, the two contributions cancel each other almost exactly. When the implicit solvent effect from COSMO is included on CPMD configurations, $^1J_{PtPt}$ increases by approximately 2200 Hz, as can be seen in Figure 8 ('0'). In the CPMD, in which the electrostatic, vibrational and solvent contributions are present, the $^1J_{PtPt}$ remains almost constant indicating that the contribution via solute-solvent interactions does not play a significant role for these complexes. This shows that obtaining the average NMR properties using a dynamic model is important for these complexes in two aspects: First, the main contribution is vibrational, which counterbalances the effect of COSMO. Second,

the contribution of solute-solvent interactions correctly describes the effect of the solvent, although the bulk effect described by COSMO contributes to overestimate the $^{1}J_{PtPt}$ in the CPMD model, suggesting that the $^{1}J_{PtPt}$ calculation using sizable clusters with a large number of solvent explicit molecules would be ideal. The computed $^{1}J_{PtPt}$ for all complexes were overestimated by 2.8 kHz on average with the CPMD approach, although the decreasing of the experimental trends is reproduced. Thus, the SSCCs in each HH system tend to decrease theoretically in the order diaquo > aquabromo > aquachloro > dichloro > dibromo, which agrees quite well with the experimental trend, where only aquabromo is switched with aquachloro.

The ZORA-SO computation yielded higher SSCCs than the ZORA-SR results (Figure 7 and Table S4) because the SO contains cross terms between diamagnetic and paramagnetic spin-orbit (DSO/PSO) coupling mechanisms and between Fermi contact and spin-dipolar (FC/SD) coupling mechanisms.[71,121] As the coupling mechanism is almost purely FC, the calculated SSCC may undergo an increase due to SO coupling.

We also compared the $^{1}J_{PtPt}$ computed applying PBE (GGA) and PBE0 (hybrid) functionals. For static geometries, the results showed that the GGA PBE functional optimized geometry and the hybrid PBE0 functional magnetic property is the best approach to obtain the accurate SSCCs. For CPMD configurations solvated with 10 NN explicit solvent molecules plus COSMO at the ZORA-SO/PBE/jcpl level of theory, the average $^{1}J_{PtPt}$ only decreases approximately 1 kHz for the diaquo complex and 530 Hz for the dihalo and aquahalo complexes (Table S5). Therefore, the protocol used in this work, where the CPMD configurations are obtained with GGA PBE functional and NMR properties are obtained using hybrid PBE0 functional, is currently the best choice for the investigated systems.

3.4.2 *J*-coupling analysis

SSCC decomposition in terms of NLMO contributions was performed to rationalize the solvent effect on the $^{1}J_{PtPt}$ coupling. The application of NLMO analysis provides a wealth of information regarding the chemical bonds in a system and their relationship to observable properties, such as NMR properties. In addition, the relationship of the NLMOs to an ideally localized set of NBOs provides insight into the extent of the electron delocalization and a chemically intuitive description of the molecular electronic structure. The analysis consists of building a set of NLMOs from a set of well localized NBOs that represent chemical bonds, lone pairs (LPs), and core (CR) and unoccupied orbitals. When the electronic structure is well localized, the NLMOs are very similar to the parent NBOs, resembling a perfect Lewis (L) structure with the occupancy of each NBO very near to 2 for the closed shell systems. When the electronic structure presents delocalization, the NLMOs have non-Lewis (NL) tails, with their

NBO occupancy less than 2.[51,104,122]

Because the observed trends for the **1** to **5** HH and HT complexes are very similar, the diaquo, dichloro and aquachloro HH complexes were chosen for investigating the $^1J_{PtPt}$ coupling transmission mechanism by NLMO analysis. Furthermore, the effect of different axial ligands, H_2O and X^-, as well as their combinations $L^1{=}L^2{=}H_2O$, $L^1{=}L^2{=}X^-$ and $L^1{=}H_2O$, $L^2{=}X^-$, may be analyzed. The analysis were performed for 64 CPMD configurations unsolvated (bare) and with complete solvation (10 NN explicit solvent molecules + COSMO). The NLMO contributions for the total $^1J_{PtPt}$ SO computation are listed in Table 2, and three of the delocalized bonding orbitals for the L^1-Pt[N_4]-Pt[N_2O_2]-L^2 moiety that feature prominently in the analysis are characterized in Table 3.

Table 2: Average contribuitions of the $^1J_{PtPt}$ NLMO analysis for Head-to-Head complexes **1**, **3** and **5**.[a]

NLMO	1		3		5	
	CPMD-Bare[b]	**CPMD**[c]	**CPMD-Bare**[b]	**CPMD**[c]	**CPMD-Bare**[b]	**CPMD**[c]
CR Pt	-2957	-2433	-1032	-1871	-633	-1927
Pt-Pt	15353	12135	1755	9612	4253	10662
LP Pt	2612	2237	1129	1725	1200	1936
LP N	-83	453	27	267	527	-50
LP O	49	-1344	61	20	-115	21
LP Cl	—	—	54	-1642	-495	-174
Pt - N	1228	917	331	351	621	-275
Pt - O	246	11	303	15	595	—
Pt - Cl	—	—	2829	388	357	320
Others	-477	549	237	778	376	245
Total	15971	12525	5692	9644	6685	10759

[a]All values (in Hz) are averaged on 64 CPMD configurations. The values are the sum of the L + NL components of each NLMO. [b]Unsolvated CPMD configurations. [c]CPMD configurations plus 10 explicit NN solvent molecules and implicit solvation to model the bulk effect.

The presence of multicenter bonding involving the axial ligands and metallic centers is observed in the NLMO set. More than 95% of the total SSCC is represented by one contribution from the Pt−Pt bonding NLMO, shown in Figure 10 for snapshots of the set of 256 extracted from the production trajectory. The NBO occupation for the sigma Pt−Pt bond is around 1.8 on average, which characterizes it as a strongly delocalized/multicenter bond, in agreement with the previous findings of related heavy atom dinuclear systems.[123,124] Other contributions are quite substantially derived from Pt, O and Cl LPs and Pt-Cl, Pt-O and Pt-N bonds. There is also a

large negative contribution from the Pt 5*s* orbital and minor contributions that were added and assigned as 'others' in Table 2.

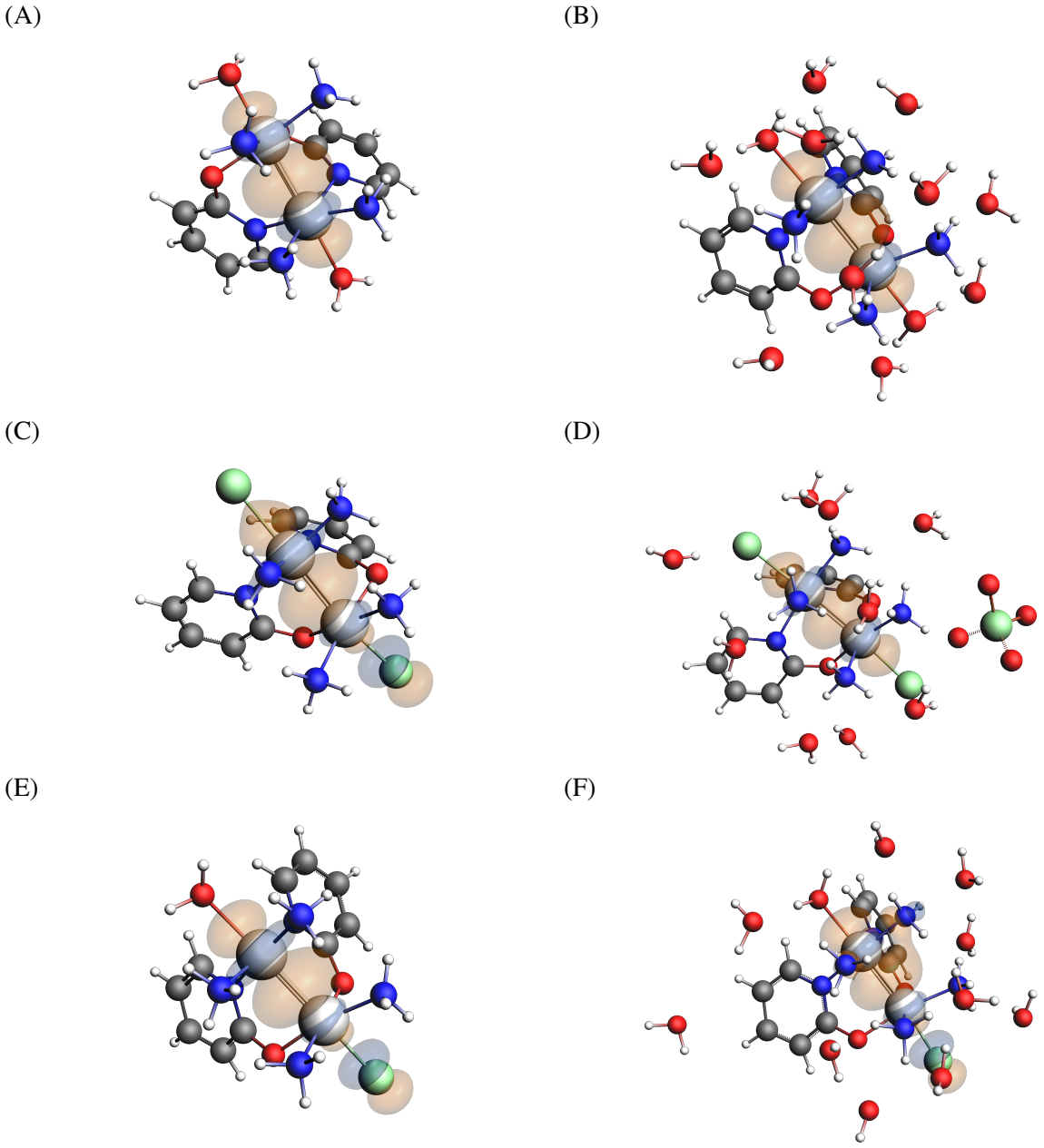

Figure 10: Snapshots from the production trajectory of HH diaquo (A,B), dichloro (C,D) and aquachloro (E,F) complexes showing the Pt−Pt bonding NLMO in the CPMD-Bare model (A,C,E) and in the CPMD model (B,D,F). The snapshots were chosen because they closely represent the MD-averaged Pt–Pt J-coupling. Isosurface values: 0.03 au.

For the diaquo complex, the solvation effect decreases the $^{1}J_{\mathrm{PtPt}}$ by approximately 3 kHz. The oxygen LP orbitals begin to contribute negatively, corresponding to 11% of the total coupling. The

Table 3: Caracterization of three delocalized bonding orbitals from the L^1-Pt[N_4]-Pt[N_2O_2]-L^2 moiety of the **1**, **3** and **5** HH complexes in terms of the weight from different atoms and *s*/*p*/*d* character.[a]

	NLMO	CPMD-Bare	CPMD
1	O_{axial}−Pt[N_4]	92 O_{axial} s(38)p(62)	90 O_{axial} s(34)p(66)
		3 Pt[N_4] s(28)p(3)d(68)	4 Pt[N_4] s(25)p(3)d(73)
		2 Pt[N_2O_2] s(19)p(3)d(77)	5 Pt[N_2O_2] s(18)p(3)d(79)
	Pt-Pt	56 Pt[N_4] s(14)d(86)	55 Pt[N_4] s(13)d(85)
		39 Pt[N_2O_2] s(17)d(82)	41 Pt[N_2O_2] s(15)d(84)
	Pt[N_2O_2]−O_{axial}	89 Oax s(44)p(56)	87 O_{axial} s(67)p(33)
		6 Pt[N_2O_2] s(21)d(77)	4 Pt[N_2O_2] s(20)d(78)
		4 Pt[N_4] s(14)p(2)d(84)	3 Pt[N_4] s(12)p(2)d(86)
3	Cl-Pt[N_4]	80 Cl s(4)p(96)	85 Cl s(7)p(93)
		7 Pt[N_2O_2] s(13)p(11)d(76)	6 Pt[N_4] s(31)p(9)d(60)
		6 Pt[N_4] s(17)p(19)d(63)	5 Pt[N_2O_2] s(16)p(8)d(77)
	Pt-Pt	72 Pt[N_4] s(8)d(91)	53 Pt[N_4] s(12)d(87)
		15 Pt[N_2O_2] s(11)p(4)d(84)	44 Pt[N_2O_2] s(15)d(85)
		11 Cl s(6)p(94)	
	Pt[N_2O_2]-Cl	54 Cl s(5)p(94)	76 Cl s(6)p(93)
		45 Pt[N_2O_2] s(14)d(86)	13 Pt[N_2O_2] s(19)d(79)
		10 Pt[N_4] s(12)p(3)d(85)	10 Pt[N_4] s(12)p(3)d(85)
5	O_{axial}−Pt[N_4]	96 O_{axial} s(25)p(75)	94 O s(23)p77)
		1 Pt[N_4] s(36)p(12)d(51)	2 Pt[N_4] s(42)p(7)d(50)
		1 Pt[N_2O_2] s(25)p(10)d(65)	2 Pt[N_2O_2] s(21)p(6)d(72)
	Pt-Pt	78 Pt[N_4] s(7)d(92)	60 Pt[N_4] s(21)d(78)
		11 Pt[N_2O_2] s(18)p(4)d(78)	19 Pt[N_2O_2] s(16)p(3)d(81)
		9 Cl[Pt] s(5)p(95)	10 Cl[Pt] s(8)p(92)
	Pt[N_2O_2]-Cl	54 Cl s(4)p(96)	63 Cl s(8)p(92)
		44 Pt[N_2O_2] s(18)d(82)	36 Pt[N_2O_2] s(17)d(82)

[a]All values (in %) are averaged on 64 CPMD configurations.

solvent effect also increases the agreement of the Pt−Pt NLMO with the parent NBO from 92% to 94%, thus indicating a more localized NLMO. In addition, the contribution of each natural atomic orbital (NAO) becomes more balanced (Table 3). However, the most dramatic solvation effect is the *s* character decrease of the Pt NAOs because it is directly related to the Fermi contact, the main mechanism responsible for the coupling. Thus, the small reduction in the *s*-character is responsible for the $^1J_{PtPt}$ coupling decrease in the solvated regime. The O_{axial}−Pt[N_4] and Pt[N_2O_2]−O_{axial} interactions were assigned to LP orbitals slightly delocalized on the Pt atoms, with similar features in unsolvated or solvated regimes, as shown in Figures S14A–S14D.

For the dihalo complex, the Pt−Pt bonding NLMO is characterized as an LP of the Pt[N_4] atom that is delocalized onto the Pt[N_2O_2] (15%) and the Cl^- (11%) atoms (Figure 10C), suggesting a weak covalent interaction between the metal centers. This NLMO contributes only 31% of the

total coupling in the CPMD-bare model. The most important contribution comes from Pt−Cl bonds, with an average of 50% for the total coupling. This happens because the Cl−Pt[N_4] and Pt[N_2O_2]−Cl bonding NLMOs are delocalized over both Pt atoms, by approximately 13% and 10% respectively, as an LP orbital and a ligand σ orbital of covalent interaction (Figures S14E and S14G, respectively).

When the solvent is present, the percent contribution from the NBO parent of the Pt−Pt bonding NLMO increases from 72% to 93%, and now 99% of the total coupling comes from this highly localized orbital. The Pt−Pt bonding NLMO does not present the three-center-four-electron character because its NAO contribution is more balanced (Figure 10D). On the other hand, the NLMO of the Cl−Pt[N_4] bond does not undergo substantial changes upon solvation (Figure S14F), while the NLMO of Pt[N_2O_2]−Cl (Figure S14H) becomes less covalent. Their contributions are also substantially decreased, by approximately 2.4 kHz, but the LP orbitals of Cl showed a remarkable negative contribution. Unlike what we observed in the diaquo complex, the Pt NAOs showed an increase in their *s*-character and hence increased the $^1J_{PtPt}$ coupling upon solvation. Therefore, the solvent effect on the dihalo complexes plays the key role of reorganizing the electronic structure and localizing the Pt−Pt bonding orbital, changing the FC mechanism.

In the aquahalo complexes, the Pt−Pt bonding NLMO is the dominant contribution to the total coupling (Figures 10E and 10F). The three-center-four-electron character is observed for the Pt−Pt and O_{axial}−Pt[N_4] (Figures S14I and S14J) NLMOs in solvated and unsolvated regimes, and unlike in dihalo complexes, the Pt[N_2O_2]−Cl bond is well localized (Figures S14K and S14L). Furthermore, the solvent effect leads to a more delocalized Pt−Pt NLMO, decreasing the percent contribution from their parent NBO from 78% to 52%. This Pt−Pt bond delocalization, which renders the three-center-four-electron character in these complexes, is consistent with experimental observations through their chemical shifts that suggest a polarization such as $X-Pt^{IV}(N_2O_2/N_3O)-Pt^{II}(N_4/N_3O)-OH_2$. In addition, the *s*-character of the Pt NAOs also undergoes a slight change, particularly in the Pt[N_4] atom, which is responsible for the increasing trend of $^1J_{PtPt}$ when NN solvent molecules are included (see Figure 8).

The *J*-coupling analysis based on canonical molecular orbitals (CMO) for larger systems typically involves a many large contributions with opposite signs,[125], which can complicate an analysis. Nevertheless, some contributions from the occupied spin-orbit CMOs (Φ) rationalize the solvent effect on the Pt^{III} complexes, as follows: For the diaquo complex (**1**) in the CPMD-Bare model, two Φ (Figure S15a) yield the main contributions to the $^1J_{PtPt}$ and the breakdown of the CMOs in terms of NLMOs shows that the first represents 88% of the Pt 5s atomic orbital, while the second contains several small contributions from different σ-bonding NLMOs of the equatorial ligands with high *p*-character, and the Pt−Pt σ-bonding NLMO as the

main component with 14%. In the CPMD model, the $^{1}J_{PtPt}$ is described by two Φ pairs (Figure S15b), both have the main contribution from Pt−Pt σ-bonding NLMO. However, the Pt 6s-character becomes more 'diluted' over the lower-energy occupied CMOs, resulting in a less efficient FC mechanism which reduces the spin-spin coupling upon explicit solvation.

For the dihalo complex (**3**) without solvent molecules, one Φ pair (Figure S16a) with main contributions from the Pt σ-lone pair and σ-bonding Pt[N_2O_2]−Cl NLMOs describes $^{1}J_{PtPt}$, both with low Pt 6s-character. In contrast, with solvent molecules two Φ pairs (Figure S16b), including the HOMO-2, have significant contributions for $^{1}J_{PtPt}$ from Pt−Pt σ-bonding NLMO (the breakdown is 64%) with high Pt 6s-character, which combined with a relatively small energy gap between the HOMO-2 and LUMO orbitals renders the FC mechanism more efficient compared with the unsolvated system. This corroborates the results from the NLMO analysis aforementioned, in which the electron density becomes more localized at the metal-metal bond and it is the key issue for the spin-spin coupling increase of these complexes.

The same characteristic of the dihalo is observed for the aquahalo (**5**) complex in the absence of the explicit solvent. The main contributions for $^{1}J_{PtPt}$ under the explicit solvent effect come from a Φ pair with 86% of Pt 5s atomic orbital character and from HOMO-3 Φ pair (Figure S17b). In this case, HOMO-3, which is described by only 14 % of Pt σ-lone pair NLMO with high Pt 6s-character, contributes less than Φ Pt 5s because the electron density in the Pt−Pt bond becomes more delocalized.

3.5 Pt^{III} Chemical Shifts

The calculated isotropic shielding constants are collected in Table S9. Also, the evolution of the shielding tensor average value was verified and 256 configurations also are a good statistic representation of the simulation. The plots are provided in Figures S18–S22. In Table 4, the NMR ^{195}Pt chemical shifts (δ^{195}Pt) obtained using static geometry with and without implicit solvation (referred to as Unsolvated and COSMO, respectively) and using explicity solvated CPMD configurations plus COSMO (referred to as CPMD) are showed. Figures 11A and 11B summarize the trends of the calculated chemical shifts in the different models used.

Table 4: Calculated ^{195}Pt chemical shift[a] for Head-to-Head (HH) and Head-to-Tail (HT) complexes **1** to **5** with different solvated and unsolvated models at the ZORA-SO/PBE0/jcpl level of theory. The values in square brackets are the absolute deviation relative to experiment.[a]

Complex		Atom	Unsolvated[b]	COSMO[c]	CPMD[d]	Exptl[e]
1	HH	Pt[N_4]	-844	-844	-844	-844
		Pt[N_2O_2]	393	393	393	393
	HT	Pt	-1482 [1217]	-1205 [940]	-245 [20]	-265
2	HH	Pt[N_4]	-891 [97]	-1767 [779]	-861 [127]	-988
		Pt[N_2O_2]	-1164 [1132]	-1085 [1053]	-5 [27]	-32
	HT	Pt	-1087 [558]	-1414 [885]	-436 [94]	-529
3	HH	Pt[N_4]	-654 [294]	-1730 [782]	-670 [278]	-948
		Pt[N_2O_2]	-1123 [1252]	-909 [1038]	163 [34]	129
	HT	Pt	-905 [472]	-1319 [886]	-294 [139]	-433
4	HH	Pt[N_4]	-1322 [69]	-1294 [97]	-269 [1122]	-1391
		Pt[N_2O_2]	-518 [1161]	-1446 [2089]	-451 [1094]	643
	HT	Pt[H_2O]	-872 [28]	-697 [203]	242 [1142]	-900
		Pt[Br]	-1033 [1053]	-1951 [1971]	-1005 [1025]	20
5	HH	Pt[N_4]	-527 [667]	-1476 [282]	-435 [759]	-1194
		Pt[N_2O_2]	-855 [1373]	-1121 [1639]	-73 [591]	518
	HT	Pt[H_2O]	-936 [284]	-821 [169]	220 [872]	-652
		Pt[Cl]	-549 [447]	-1713 [1611]	-808 [706]	-102
Mean Absolute Deviation[a]			674	962	535	

[a] All values are given in ppm, and spin-orbit corrections are included for all calculations.
[b] Relativistic chemical shifts from the unsolvated, relativistically optimized geometry.
[c] Relativistic chemical shifts from the relativistically optimized geometry with implicit solvation.
[d] Average of 256 CPMD configurations plus 10 explicit nearest neighboring solvent molecules and implicit solvation to model the bulk effect. [e] Ref. [24]

Overall, the CPMD affords δ^{195}Pt with good accuracy for HH/HT diaquo and dihalo complexes. For the HH/HT aquahalo complexes, only δ^{195}Pt for Pt[N_4]/Pt[H_2O] has a good accuracy, specifically for Unsolvated and COSMO models. This may be correlated with the large polarization of Pt−Pt bond of the aquahalo complexes ($X-Pt^{IV}(N_2O_2/N_3O)-Pt^{II}(N_4/N_3O)-OH_2$) compared to diaquo and dihalo complexes. Nonetheless, some insight can be obtained. For

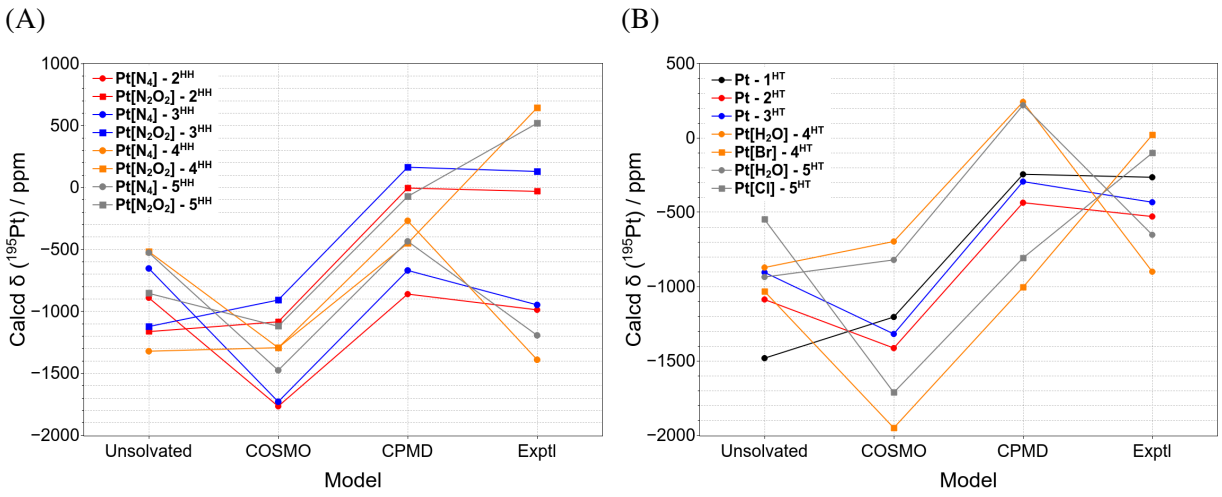

Figure 11: Trends of the NMR ^{195}Pt chemical shifts of Head-to-Head (A) and Head-to-Tail (B) complexes calculated using different models

instance, the Pt[N_2O_2] of the dibromo (**2**$^{\mathbf{HH}}$) and dichloro (**3**$^{\mathbf{HH}}$), and Pt of the diaquo (**1**$^{\mathbf{HT}}$) complexes shift to lower fields and their δ^{195}Pt show an improvement from Unsolvated to COSMO model. Then, they shift to much lower fields, agreeing with experimental values in the CPMD model, and suggesting an additional contribution from explicit and implicit solvent. On the other hand, for the other δ^{195}Pt the COSMO model worsens the agreement with the experiment. However, in the CPMD model, these δ^{195}Pt match fairly well with the experiment. The results still suggest that some error cancellation is taking place in the Unsolvated model. Because of the error cancellation, the Unsolvated model appears to perform as well as the CPMD model, for the Pt[N_4] of the **2**$^{\mathbf{HH}}$, **3**$^{\mathbf{HH}}$ and **5**$^{\mathbf{HH}}$, the Pt[N_2O_2] of the **4**$^{\mathbf{HH}}$, Pt[Br] of the **4**$^{\mathbf{HT}}$ and Pt[Cl] of the **5**$^{\mathbf{HT}}$. The mean absolute deviation (MAD) in Table 4 indicates that the Unsolvated model performs slightly better than COSMO, with a MAD of 674 ppm against 962 ppm, respectively, while the CPMD gives a MAD of 535 ppm. These differences arise from the shortcoming of the static approach in neglecting vibrational and explicit solvent contribution, which is corrected by the CPMD approach. These aforementioned observations reflect results discussed earlier for other platinum complexes,[12,59] which highlight the general difficulty of reproducing Pt NMR shifts by calculations. It is worth mentioning that the shifts obtained for compounds **4**$^{\mathbf{HT}}$ and **5**$^{\mathbf{HT}}$ in the CPMD model seem to be inverted when compared with experimental data, which were assigned based on the results of the HH aquahalo complexes considering the similarity of the Pt−Pt and Pt−N couplings.[24] Thus, our findings suggest that both Pt[X] and Pt[H_2O] may have been assigned interchangeably.

Figure 12A shows the correlation between experimental and calculated NMR ^{195}Pt chemical

shifts of the Pt^{III} complexes compared with Pt^{II}/Pt^{IV} complexes previous reported by Truflandier et al.[58,59]. A good correlation can be observed for the HH/HT diaquo and dihalo complexes, whereas for HH/HT aquahalo complexes several large disagreements were obtained. Apart from these outliers, the correlation appears to be reasonable ($R^2 = 0.98$) at the scale of the plot, as well as observed for Pt^{II}/Pt^{IV} complexes. Despite the discrepancies in the aquahalo complex data, which need further investigation, the CPMD model still yields the best results, as can be seen in Figure 12B that shows the correlation between experimental and calculated δ^{195}Pt using the three models.

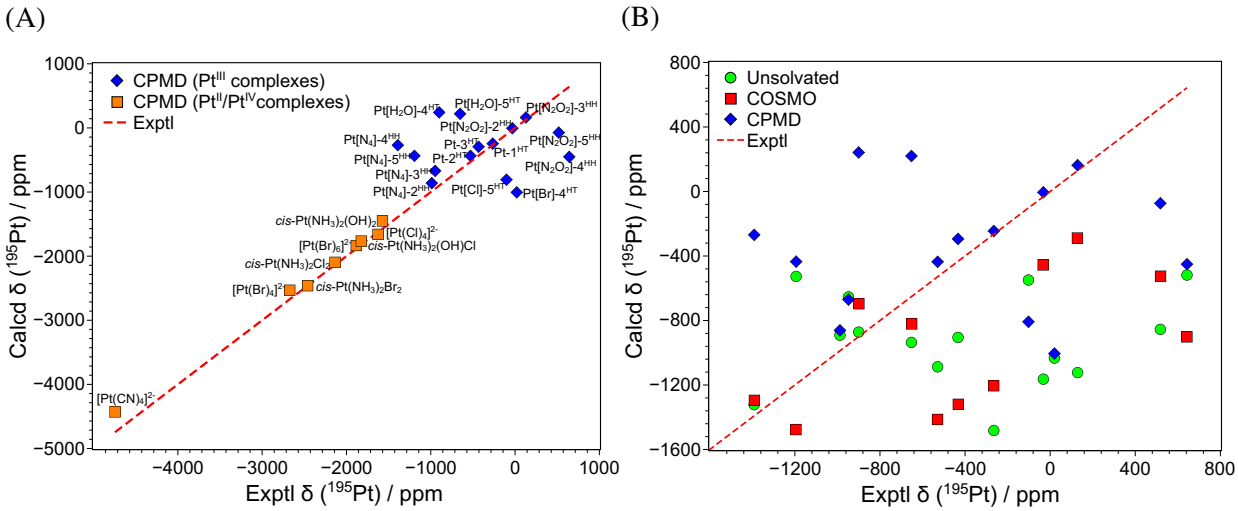

Figure 12: Correlation between experimental and calculated NMR ^{195}Pt chemical shifts with CPMD averaging protocol compared with previous work (orange rectangles)[58,59] (A); and with the other approaches used in this work (B).

The δ^{195}Pt as well as the SSCCs averaged over CPMD configurations solvated with 10 NN explicit solvent molecules plus COSMO were also computed at the ZORA-SO/PBE/jcpl level of theory (Table S6), and accuracy improvement was not observed in comparison with the results obtained at ZORA-SO/PBE0/jcpl. The chemical shift accuracy may be improved because approximations with respect to the DFT method and the basis set are always the most crucial points in theoretical calculations. The use of a hybrid functional also in the CPMD in conjunction with property calculations would be very interesting and could potentially improve the results. However, such calculations would be extremely demanding of computational resources.

4 Conclusions

In the present work, we elucidated the dynamic solvent effect on the Pt−Pt spin-spin coupling constants and ^{195}Pt chemical shifts of pyridonate-bridged Pt^{III} dinuclear complex derivatives, combining the CPMD approach and relativistic KS-DFT NMR calculations. Based on physically significant simulations, structural and molecular orbital properties that play a key role in spectroscopy are predicted with reasonable precision.

The O−O RDFs exhibit structuring similar to that of pure water,[111] indicating that complexes of this size are well solvated by 64 solvent molecules used for dynamics. The Pt−O RDFs show that the complexes have two well structured solvation shells with 10 and 30 solvent molecules. Other structural results of the complexes are in good agreement with the experimental X-ray data,[24] with some differences due to the solute-solvent interaction, primarily via hydrogen bonds.

The trends in the Pt−Pt and Pt−L bond lengths reveal a strong *trans* influence effect in solution, which is responsible for two main features of the HT complexes. First, the Pt−Pt bonds are more polarized in the aquahalo complexes than in the diaquo and dihalo complexes. Second, the probability of rotation around the Pt−Pt bond increases, which favors a *synclinal* geometry. These features are further enhanced because the bridging ligand symmetry contributes to two perfect octahedral stacked systems, where the *trans* effect is known to be more pronounced. In HH systems, the *trans* effect is reduced, and the complexes assume a twisted geometry when the metal-metal bond is elongated because of the bridging ligand asymmetry, which makes rotation around the Pt−Pt bond difficult.

The Pt−Pt SSCCs computed from snapshots along the CPMD trajectory, including SO effects, produce a difference of 2.8 kHz, on average, between theory and experiment. These results highlight the difficulty of assessing NMR Pt properties, even when important effects are included. However, some of the important experimentally observed trends were reproduced, and the role of the solvent and the solvation shell on the $^1J_{PtPt}$ could be explored and evaluated in detail. Calculations using a nonhybrid functional or scalar relativistic correction yielded acceptable agreement with experimental SSCCs because of a cancellation of errors resulting from approximations in the computational model. Without the SO calculations, a comparison between SR calculations and experiments could thererefore lead to the incorrect conclusion that the SO effects are negligible. However, this is not true for Pt^{III} complexes. Despite the overestimation of the SSCCs computed in the present work, so far there is no evidence in the literature that would point to the treatment of relativity by ZORA as the major source of errors. The observed deviations between calculated and measured NMR data therefore most likely arise from the other approximations used for the molecular dynamics and the NMR calculations, such

as finite configuration sampling, finite basis errors, and the approximations in the XC functional.

A decomposition of the electronic structures and Pt−Pt *J*-couplings reveals that, in the unsolvated and solvated regimes, three-center-four-electron Pt−Pt bonding occurs in the diaquo and aquahalo complexes. The presence of explicit solvation makes the NLMOs more localized in the diaquo and dihalo complexes, improving the Pt−Pt coupling. For the diaquo complex, the solvent effect reduces the *s*-character in the Pt−Pt bond, whereas for the dihalo and aquahalo complexes, the *s* character increases. These main findings of the analysis rationalize the dramatic decrease in $^{1}J_{\mathrm{PtPt}}$ due to solvation, in particular, for the diaquo complex, and the pronounced increase in $^{1}J_{\mathrm{PtPt}}$ for dihalo and aquahalo complexes, affecting the Fermi contact *J*-coupling mechanism.

$^{195}\mathrm{Pt}^{\mathrm{III}}$ chemical shifts present a variation of values within the different models evaluated, and the agreement with experiment has room for improvement. However, the chemical shifts computed from CPMD snapshots show good improvement with respect to those computed from unsolvated static geometries. In most cases, the accuracy of the MD-averaged shifts is better than or similar to those obtained using static geometries with COSMO.

The present calculations also show that modern techniques, combining relativistic electronic structure methods with ab-initio molecular dynamics and on-the-fly analysis of the calculated NMR tensors are able to give unprecedented detailed insight into the factors that determine the experimental observations at the microscopic level.

Supporting Information Available

Additional radial distribution functions of the solvent and solute, CPMD structural parameters of the solute, isotropic shielding values, dynamic properties, relativistic scalar corrections on the $^{1}J_{\mathrm{PtPt}}$ results of NMR properties computed with CPMD configurations using a nonhybrid functional, assessment of the DFT functional, canonical molecular orbitals, the evolution of the average of the shielding tensor and coordinates of atomic positions of the last snapshot from CPMD equilibration trajectory.

Author contributions

P.R.B. performed the calculations. All authors contributed to the analysis and discussions of the results, preparation and revision of the manuscript.

Conflicts of Interest

There are no conflicts to declare

Acknowledgments

We acknowledge the National Laboratory for Scientific Computing (LNCC/MCTI, Brazil, SDumont supercomputer) and Center for Computational Research (CCR) at the University at Buffalo for providing HPC resources. L.C.D. and P.R.B. acknowledge grants #2017/17750-3, #2018/07308-4, São Paulo Research Foundation (FAPESP). L.C.D. is also acknowledge CNPq #306844/2020-6 grant. J.A. is grateful for support by National Science Foundation, grant CHE-1855470.

References

(1) P. S. Pregosin, *Annu. Rep. NMR. Spectros.*, 1986, **17**, 285–349.

(2) P. S. Pregosin, *Coord. Chem. Rev.*, 1982, **44**, 247–291.

(3) B. M. Still, P. G. A. Kumar, J. R. Aldrich-Wright and W. S. Price, *Chem. Soc. Rev.*, 2007, **36**, 665–686.

(4) T. M. Gilbert and T. Ziegler, *J. Phys. Chem. A*, 1999, **103**, 7535–7543.

(5) A. Buckingham, T. Schaefer and W. Schneider, *J. Chem. Phys.*, 1960, **32**, 1227–1233.

(6) R. Ghanghas, A. Jindal and S. Vasudevan, *J. Phys. Chem. B*, 2018, **122**, 9757–9762.

(7) L. Engelbrecht, F. Mocci, A. Laaksonen and K. R. Koch, *Inorg. Chem.*, 2018, **57**, 12025–12037.

(8) A. Ruh and V. G. Kiselev, *J. Magn. Reson.*, 2019, **307**, 106584.

(9) J. Autschbach and T. Ziegler, *J. Am. Chem. Soc.*, 2001, **123**, 5320–5324.

(10) E. P. Fowe, P. Belser, C. Daul and H. Chermette, *Phys. Chem. Chem. Phys.*, 2005, **7**, 1732–1738.

(11) J. Autschbach and B. Le Guennic, *Chem. Eur. J.*, 2004, **10**, 2581–2589.

(12) M. Sterzel and J. Autschbach, *Inorg. Chem.*, 2006, **45**, 3316–3324.

(13) J. C. Davis, M. Bühl and K. R. Koch, *J. Chem. Theory Comput.*, 2012, **8**, 1344–1350.

(14) J. Barton, H. Rabinowitz, D. Szalda and S. Lippard, *J. Am. Chem. Soc.*, 1977, **99**, 2827–2829.

(15) J. K. Barton, D. J. Szalda, H. N. Rabinowitz, J. V. Waszczak and S. J. Lippard, *J. Am. Chem. Soc.*, 1979, **101**, 1434–1441.

(16) T. V. O'Halloran and S. J. Lippard, *Isr. J. Chem.*, 1985, **25**, 130–137.

(17) J. J. Wilson and S. J. Lippard, *Inorg. Chem.*, 2012, **51**, 9852–9864.

(18) L. S. Hollis and S. J. Lippard, *J. Am. Chem. Soc.*, 1981, **103**, 6761–6763.

(19) J. Schagen, A. Overbeek and H. Schenk, *Inorg. Chem.*, 1978, **17**, 1938–1940.

(20) C. Bellitto, A. Flamini, L. Gastaldi and L. Scaramuzza, *Inorg. Chem.*, 1983, **22**, 444–449.

(21) F. A. Cotton, L. R. Falvello and S. Han, *Inorg. Chem.*, 1982, **21**, 2889–2891.

(22) R. El-Mehdawi, F. R. Fronczek and D. M. Roundhill, *Inorg. Chem.*, 1986, **25**, 1155–1159.

(23) J. D. Woollins and P. F. Kelly, *Coord. Chem. Rev.*, 1985, **65**, 115–140.

(24) S. Iwatsuki, E. Isomura, A. Wada, K. Ishihara and K. Matsumoto, *Eur. J. Inorg. Chem.*, 2006, **2006**, 2484–2490.

(25) K. Matsumoto and K. Sakai, *Adv. Inorg. Chem.*, Elsevier, 1999, vol. 49, pp. 375–427.

(26) J. P. Davidson, P. J. Faber, J. R. Fischer, S. Mansy, H. J. Peresie, B. Rosenberg and L. VanCamp, *Cancer Chemother. Rep.*, 1975, **59**, 287–300.

(27) R. Speer, H. Ridgway, L. Hall, D. Stewart, K. Howe, D. Lieberman, A. Newman and J. Hill, *Cancer Chemother. Rep.*, 1975, **59**, 629–641.

(28) J. Matsunami, H. Urata and K. Matsumoto, *Inorg. Chem.*, 1995, **34**, 202–208.

(29) B. Rosenberg, L. Van Camp and T. Krigas, *Nature*, 1965, **205**, 698–699.

(30) B. Rosenberg, L. Vancamp, J. E. Trosko and V. H. Mansour, *Nature*, 1969, **222**, 385–386.

(31) B. Rosenberg and L. VanCamp, *Cancer Res.*, 1970, **30**, 1799–1802.

(32) S. J. Lippard, *Science*, 1982, **218**, 1075–1082.

(33) K. Sakai, Y. Tanaka, Y. Tsuchiya, K. Hirata, T. Tsubomura, S. Iijima and A. Bhattacharjee, *J. Am. Chem. Soc.*, 1998, **120**, 8366–8379.

(34) K. Sakai, E. Ishigami, Y. Konno, T. Kajiwara and T. Ito, *J. Am. Chem. Soc.*, 2002, **124**, 12088–12089.

(35) M. Yoshida, N. Yashiro, H. Shitama, A. Kobayashi and M. Kato, *Chem. Eur. J.*, 2016, **22**, 491–495.

(36) T. M. Swager, *Acc. Chem. Res.*, 1998, **31**, 201–207.

(37) X. Wu, D.-G. Chen, D. Liu, S.-H. Liu, S.-W. Shen, C.-I. Wu, G. Xie, J. Zhou, Z.-X. Huang, C.-Y. Huang *et al.*, *J. Am. Chem. Soc.*, 2020, **142**, 7469–7479.

(38) A. Stiegman, V. Miskowski and H. B. Gray, *J. Am. Chem. Soc.*, 1986, **108**, 2781–2782.

(39) K. Matsumoto and K. Sakai, *Adv. Inorg. Chem.*, 2000, **49**, 375–427.

(40) M. A. Bennett, S. K. Bhargava, E. C.-C. Cheng, W. H. Lam, T. K.-M. Lee, S. H. Privér, J. Wagler, A. C. Willis and V. W.-W. Yam, *J. Am. Chem. Soc.*, 2010, **132**, 7094–7103.

(41) T. Appleton, H. Clark and L. Manzer, *Coord. Chem. Rev.*, 1973, **10**, 335–422.

(42) A. Greif, P. Hrobarik, A. Arbuznikov, J. Autschbach and M. Kaupp, *Inorg. Chem.*, 2015, **54**, 7199–7208.

(43) J. NovotnÃ¡, J. VÃŋcha, P. L. Bora, M. Repisky, M. Straka, S. Komorovsky and R. Marek, *J. Chem. Theory. Comput.*, 2017, **13**, 3586–3601.

(44) J. Vícha, J. Novotný, S. Komorovsky, M. Straka, M. Kaupp and R. Marek, *Chem. Rev.*, 2020, **120**, 7065–7103.

(45) M. Bühl and F. T. Mauschick, *Phys. Chem. Chem. Phys.*, 2002, **4**, 5508–5514.

(46) M. Bühl, F. T. Mauschick, F. Terstegen and B. Wrackmeyer, *Angew. Chem. Int. Ed.*, 2002, **41**, 2312–2315.

(47) M. Bühl, *J. Phys. Chem. A*, 2002, **106**, 10505–10509.

(48) M. Buehl, R. Schurhammer and P. Imhof, *J. Am. Chem. Soc.*, 2004, **126**, 3310–3320.

(49) M. Bühl, S. Grigoleit, H. Kabrede and F. T. Mauschick, *Chem. Eur. J.*, 2006, **12**, 477–488.

(50) R. Car and M. Parrinello, *Phys. Rev. Lett.*, 1985, **55**, 2471–2474.

(51) S. Zheng and J. Autschbach, *Chem. Eur. J.*, 2011, **17**, 161–173.

(52) T. M. Alam, D. Hart and S. L. Rempe, *Phys. Chem. Chem. Phys.*, 2011, **13**, 13629–13637.

(53) M. Dračínskỳ, H. M. Möller and T. E. Exner, *J. Chem. Theory. Comput.*, 2013, **9**, 3806–3815.

(54) A. C. Castro, H. Fliegl, M. Cascella, T. Helgaker, M. Repisky, S. Komorovsky, M. Á. Medrano, A. G. Quiroga and M. Swart, *Dalton Trans.*, 2019, **48**, 8076–8083.

(55) L. Halbert, M. Olejniczak, V. Vallet and A. Severo Pereira Gomes, *Int. J. Quantum Chem.*, 2019, e26207.

(56) L. C. Ducati, A. Marchenko and J. Autschbach, *Inorg. Chem.*, 2016, **55**, 12011–12023.

(57) S. Moncho and J. Autschbach, *J. Chem. Theory Comput.*, 2010, **6**, 223–234.

(58) L. A. Truflandier and J. Autschbach, *J. Am. Chem. Soc.*, 2010, **132**, 3472–3483.

(59) L. A. Truflandier, K. Sutter and J. Autschbach, *Inorg. Chem.*, 2011, **50**, 1723–1732.

(60) K. Sutter, L. A. Truflandier and J. Autschbach, *ChemPhysChem*, 2011, **12**, 1448–1455.

(61) N. Saeki, Y. Hirano, Y. Sasamoto, I. Sato, T. Toshida, S. Ito, N. Nakamura, K. Ishihara and K. Matsumoto, *Bull. Chem. Soc. Jpn*, 2001, **74**, 861–868.

(62) N. Saeki, Y. Hirano, Y. Sasamoto, I. Sato, T. Toshida, S. Ito, N. Nakamura, K. Ishihara and K. Matsumoto, *Eur. J. Inorg. Chem.*, 2001, **2001**, 2081–2088.

(63) M. Arime, K. Ishihara and K. Matsumoto, *Inorg. Chem.*, 2004, **43**, 309–316.

(64) N. Saeki, N. Nakamura, T. Ishibashi, M. Arime, H. Sekiya, K. Ishihara and K. Matsumoto, *J. Am. Chem. Soc.*, 2003, **125**, 3605–3616.

(65) K. Shimazaki, H. Sekiya, H. Inoue, N. Saeki, K. Ishihara and K. Matsumoto, *Eur. J. Inorg. Chem.*, 2003, **2003**, 1785–1793.

(66) T. Terada, Y. Kamezaki, R. Nakamura, T. Sugaya, S. Iwatsuki, K. Ishihara and K. Matsumoto, *Inorganica Chim. Acta*, 2017, **467**, 391–399.

(67) S. Kusuhara, K. Kojima, Y. Suzuki, Y. Morita, T. Sugaya, S. Iwatsuki, K. Ishihara and K. Matsumoto, *J. Mol. Liq.*, 2018, **262**, 556–564.

(68) Y. Ito, K. Yamashima, S. Arai, M. Takahashi, T. Itou, S. Iwatsuki, K. Ishihara and K. Matsumoto, *Inorganica Chim. Acta*, 2020, **513**, 119934.

(69) P. Giannozzi, S. Baroni, N. Bonini, M. Calandra, R. Car, C. Cavazzoni, D. Ceresoli, G. L. Chiarotti, M. Cococcioni, I. Dabo, A. D. Corso, S. de Gironcoli, S. Fabris, G. Fratesi, R. Gebauer, U. Gerstmann, C. Gougoussis, A. Kokalj, M. Lazzeri, L. Martin-Samos, N. Marzari, F. Mauri, R. Mazzarello, S. Paolini, A. Pasquarello, L. Paulatto, C. Sbraccia, S. Scandolo, G. Sclauzero, A. P. Seitsonen, A. Smogunov, P. Umari and R. M. Wentzcovitch, *J. Phys. Cond. Mat.*, 2009, **21**, 395502.

(70) J. Autschbach and T. Ziegler, *J. Chem. Phys.*, 2000, **113**, 936–947.

(71) J. Autschbach and T. Ziegler, *J. Chem. Phys.*, 2000, **113**, 9410–9418.

(72) A. Devarajan, A. Gaenko and J. Autschbach, *J. Chem. Phys.*, 2009, **130**, 194102.

(73) G. Schreckenbach and T. Ziegler, *J. Phys. Chem.*, 1995, **99**, 606–611.

(74) S. K. Wolff, T. Ziegler, E. van Lenthe and E. J. Baerends, *J. Chem. Phys.*, 1999, **110**, 7689–7698.

(75) E. Zurek and T. Ziegler, *Faraday Discuss.*, 2003, **124**, 93–109.

(76) G. te Velde, F. M. Bickelhaupt, E. J. Baerends, C. Fonseca Guerra, S. J. A. van Gisbergen, J. G. Snijders and T. Ziegler, *J. Comput. Chem.*, 2001, **22**, 931–967.

(77) E. J. Baerends, T. Ziegler, J. Autschbach, D. Bashford, A. Bérces, F. M. Bickelhaupt, C. Bo, P. M. Boerrigter, L. Cavallo, D. P. Chong, L. Deng, R. M. Dickson, D. E. Ellis, M. van Faassen, L. Fan, T. H. Fischer, C. Fonseca Guerra, A. Ghysels, A. Giammona, S. J. A. van Gisbergen, A. W. Götz, J. A. Groeneveld, O. V. Gritsenko, M. Grüning, S. Gusarov, F. E. Harris, P. van den Hoek, C. R. Jacob, H. Jacobsen, L. Jensen, J. W. Kaminski, G. van Kessel, F. Kootstra, A. Kovalenko, M. V. Krykunov, E. van Lenthe, D. A. McCormack, A. Michalak, M. Mitoraj, J. Neugebauer, V. P. Nicu, L. Noodleman, V. P. Osinga, S. Patchkovskii, P. H. T. Philipsen, D. Post, C. C. Pye, W. Ravenek, J. I. Rodríguez, P. Ros, P. R. T. Schipper, G. Schreckenbach, J. S. Seldenthuis, M. Seth, J. G. Snijders, M. Solà, M. Swart, D. Swerhone, G. te Velde, P. Vernooijs, L. Versluis, L. Visscher, O. Visser, F. Wang, T. A. Wesolowski, E. M. van Wezenbeek, G. Wiesenekker, S. K. Wolff, T. K. Woo and A. L. Yakovlev, *Amsterdam Density Functional, SCM, Theoretical Chemistry, Vrije Universiteit, Amsterdam, The Netherlands.*, https://www.scm.com, URL https://www.scm.com. Accessed 03/17.

(78) R. A. DiStasio Jr., B. Santra, Z. Li, X. Wu and R. Car, *J. Chem. Phys.*, 2014, **141**, 84502.

(79) L. Martínez, R. Andrade, E. G. Birgin and J. M. Martínez, 2009, **30**, 2157–2164.

(80) J. M. Martínez and L. Martínez, *J. Comput. Chem.*, 2003, **24**, 819–825.

(81) J. P. Perdew, K. Burke and M. Ernzerhof, *Phys. Rev. Lett.*, 1996, **77**, 3865–3868.

(82) A. Dal Corso, *Comput. Mater. Sci.*, 2014, **95**, 337–350.

(83) S. Grimme, *Angew. Chem. Int. Edit.*, 2008, **47**, 3430–3434.

(84) M. E. Tuckerman and M. Parrinello, *J. Chem. Phys.*, 1994, **101**, 1302.

(85) M. E. Tuckerman and M. Parrinello, *J. Chem. Phys.*, 1994, **101**, 1316–1329.

(86) S. Nosé, *J. Chem. Phys.*, 1984, **81**, 511.

(87) M. V. Fernández-Serra and E. Artacho, *J. Chem. Phys.*, 2004, **121**, 11136–11144.

(88) P. H.-L. Sit and N. Marzari, *J. Chem. Phys.*, 2005, **122**,.

(89) H. S. Lee and M. E. Tuckerman, *J. Chem. Phys.*, 2007, **126**, 164501–16.

(90) W. Humphrey, A. Dalke and K. Schulten, *J. Mol. Graph.*, 1996, **14**, 33–38.

(91) B. G. Levine, J. E. Stone and A. Kohlmeyer, *J. Comput. Phys.*, 2011, **230**, 3556–3569.

(92) C. Adamo and V. Barone, *J. Chem. Phys.*, 1999, **110**, 6158–6170.

(93) E. van Lenthe and E. J. Baerends, *J. Chem. Phys.*, 2000, **112**, 8279–8292.

(94) J. Autschbach, *ChemPhysChem*, 2009, **10**, 2274–2283.

(95) J. Autschbach, *Theor. Chem. Acc.*, 2004, **112**, 52–57.

(96) J. Autschbach, *Mol. Phys.*, 2013, **111**, 2544–2554.

(97) V. Arcisauskaite, J. I. Melo, L. Hemmingsen and S. P. A. Sauer, *J. Chem. Phys.*, 2011, **135**, 044306–11.

(98) A. Wodynski, M. Repisky and M. Pecul, *J. Chem. Phys.*, 2012, **137**, 014311–11.

(99) A. Klamt, *J. Phys. Chem.*, 1995, **99**, 2224–2235.

(100) J.P. Perdew, A. Zunger, *Phys. Rev. B*, 1981, **23**, 5048–5079.

(101) A. D. Becke, *J. Chem. Phys.*, 1993, **98**, 5648–5652.

(102) M. D. Hanwell, D. E. Curtis, D. Lonie, T. Vandermeersch, E. Zurek and G. R. Hutchison, *J. Cheminf.*, 2012, **4**, 1–17.

(103) E. D. Glendening, C. R. Landis and F. Weinhold, *J. Comput. Chem.*, 2013, **34**, 1429–1437.

(104) J. Autschbach, *J. Chem. Phys.*, 2007, **127**, 124106.

(105) J. Autschbach, *J. Chem. Phys.*, 2008, **128**, 164112.

(106) A. Soper and M. Phillips, *Chem. Phys.*, 1986, **107**, 47–60.

(107) A. Soper, *Chem. Phys.*, 2000, **258**, 121–137.

(108) G. Hura, D. Russo, R. M. Glaeser, T. Head-Gordon, M. Krack and M. Parrinello, *Phys. Chem. Chem. Phys.*, 2003, **5**, 1981–1991.

(109) J. A. Morrone and R. Car, *Phys. Rev. Lett.*, 2008, **101**, 017801.

(110) J. M. Sorenson, G. Hura, R. M. Glaeser and T. Head-Gordon, *J. Chem. Phys.*, 2000, **113**, 9149–9161.

(111) A. K. Soper and C. J. Benmore, *Phys. Rev. Lett.*, 2008, **101**, 065502.

(112) M. Mitchell, B. Muftakhidinov, T. Winchen, Z. Jędrzejewski-Szmek, T. G. Badger and badshah400, *markummitchell/engauge-digitizer: Version 10.4*, 2017.

(113) T. Steiner, *Angew. Chem. Int. Ed.*, 2002, **41**, 48–76.

(114) L. S. Hollis and S. J. Lippard, *Inorg. Chem.*, 1983, **22**, 2605–2614.

(115) L. S. Hollis, M. M. Roberts and S. J. Lippard, *Inorg. Chem.*, 1983, **22**, 3637–3644.

(116) K. Sakai, I. Sakai, T. Kajiwara and T. Ito, *Acta Cryst. E*, 2004, **60**, 255–258.

(117) T. V. O'Halloran and S. J. Lippard, *Isr. J. Chem.*, 1985, **25**, 130–137.

(118) M. P. Mitoraj, H. Zhu, A. Michalak and T. Ziegler, *Int. J. Quantum Chem.*, 2009, **109**, 3379–3386.

(119) K. Sakai, T. Sakamoto, T. Kajiwara and T. Ito, *Acta Cryst. E*, 2003, **59**, m553–m555.

(120) H. Flyvbjerg and H. G. Petersen, *J. Chem. Phys.*, 1989, **91**, 461–466.

(121) S. Kirpekar and S. P. A. Sauer, *Theor. Chem. Acc.*, 1999, **103**, 146–153.

(122) S. J. Wilkens, W. M. Westler, J. L. Markley and F. Weinhold, *J. Am. Chem. Soc.*, 2001, **123**, 12026–12036.

(123) B. Le Guennic, K. Matsumoto and J. Autschbach, *Magn. Reson. Chem.*, 2004, **42**, S99–S116.

(124) J. Autschbach and S. Zheng, *Magn. Reson. Chem.*, 2008, **46**, S48–S55.

(125) J. Autschbach and B. Le Guennic, *J. Chem. Educ.*, 2007, **84**, 156–171.